The Thesis commitee of Malik Hassanaly
certifies that this is the approved version of the following thesis:

Large Eddy Simulations (LES) of boundary layer flashback in wall-bounded flows

APPROVED BY

SUPERVISING COMMITTEE:

———————————————————————
Noel Clemens, Supervisor

———————————————————————
Venkat Raman

Large Eddy Simulations (LES) of boundary layer flashback in wall-bounded flows

by

Malik Hassanaly

THESIS

Presented to the Faculty of the Graduate School of

The University of Texas at Austin

in Partial Fulfillment

of the Requirements

for the Degree of

Master of Science in Engineering

THE UNIVERSITY OF TEXAS AT AUSTIN

December 2014

To my exemplary sister

Acknowledgments

I wish to first thank my advisor Prof. Venkat Raman who offered me the opportunity to join the Aerospace graduate program at UT, for his guidance over these past two years. I would like to particularly thank him for his patience and the motivation he was able to give me at anytime. His advices on many different levels have been and will be extremely precious. Thanks also to Prof. Noel Clemens for accepting to be a committee member.

I would like to also thank Christopher Lietz for his continuous involvement with the project and all the insightful conversations we have had, usually at night for some reason.

I will also particularly thank Dr. Heeseok Koo who has been there to answer my numerous questions from my very first day in the research group. I dream of a world where every professor could be as gifted as him.

Many thanks to my family, my close friends.

Finally thanks to the past and current French governments, who understood how crucial is a free access to education.

Large Eddy Simulations (LES) of boundary layer flashback in wall-bounded flows

Malik Hassanaly, M.S.E.
The University of Texas at Austin, 2014

Supervisor: Noel Clemens

In the design of high-hydrogen content gas turbines for power generation, flashback of the turbulent flame by propagation through the low velocity boundary layers in the premixing region is an operationally dangerous event. The high reactivity of hydrogen combined with enhanced flammability limits (compared to natural gas) promotes flame propagation along low-speed boundary layers adjoining the combustion walls.

This work focuses on the simulation of boundary layer flashback using large-eddy simulations (LES). A canonical channel configuration is studied to assess the capabilities of LES and determine the modeling requirements for boundary layer flashback simulations. To extend this work to complex geometries, a new reactive low-Mach number solver has been written in an unstructured code.

Nomenclature

Abreviations

BLF   **B**oundary **L**ayer **F**lashback

DNS   **D**irect **N**umerical **S**imulations

IGCC   **I**ntegrated **G**asification **C**ombined **C**ycle

LES   **L**arge **E**ddy **S**imulations

MMS   **M**ethod of **M**anufactured **S**olutions

RANS   **R**eynolds **A**verage **N**avier-**S**tokes

Greek Symbols

$\boldsymbol{\phi}$ Array of transported scalars

η Kolmogorov length scale $[m]$

ϕ Any scalar

ρ Density $[kg.m^{-3}]$

Other Symbols

$(.)_{\mathbf{i}}$ Coordinate i of the vector $(.)$

$\cdot$ Inner product operator

$\Im_u$ Unclosed subgrid scale terms of the momentum conservation equation $[kg.m^{-2}.s^{-2}]$

$\Im_\phi$ Unclosed subgrid scale terms of the scalar conservation equation $[kg.m^{-3}.s^{-1}]$

∇ Gradient operator $[m^{-1}]$

$\overline{(.)}$ Space filtered variable or linear interpolation of cell centered values to the cell faces

$\widetilde{(.)}$ Favre filtered variable

Roman Symbols

I   Identity tensor, $I_{ij} = \delta_{ij}$

S   Strain-rate tensor, $S_{ij} = \frac{1}{2}(\frac{\partial u_i}{\partial x_j} + \frac{\partial u_j}{\partial x_i})$ $[s^{-1}]$

u   Velocity vector $[m.s^{-1}]$

D Diffusivity $[m^2.s^{-1}]$

p Fluctuating pressure $[kg.m^{-1}.s^{-2}]$

s_L Laminar flame speed $[m.s^{-1}]$

s_T Turbulent flame speed $[m.s^{-1}]$

$S_{Channel}$ Surface area of a channel YZ plane $[m^2]$

S_{Flame} Surface area of the flame $[m^2]$

t Time $[s]$

U_{FLBK} Flashback velocity $[m.s^{-1}]$

Re   Reynolds number

Table of Contents

List of Figures

Chapter 1

Introduction

1.1 Pre-combustion carbon capture for reducing greenhouse emissions

CO_2 is the primary driver of greenhouse gases based global warming that is causing significant changes to the global climate. One of the main sources of CO_2 emissions is from the burning of coal to generate electricity. In order to balance the abundant supply of coal in the US with the need to curb emissions, alternate means of coal utilization are being actively sought. One such technology is pre-combuston carbon capture, whereby coal is processed by passing steam over a coal-bed to generate a mixture of carbon monoxide and hydrogen called syngas. The carbon monoxide could then be removed through a scrubbing process to produce hydrogen that is burned in conventional stationary power turbines. Since the scrubbing process requires energy, complete CO removal is forsaken to gain efficiency of the overall process. As a result, the power turbines burn a syngas mixture with variable amounts of CO. Such systems are part of the integrated gasification combined cycle (IGCC) power plants and are promoted by the US Department of Energy as a means to clean utilization of coal. The scrubbed CO is stored in a separate carbon sequestration cycle.

Although syngas has been widely used for combustion for more than a hundred years, its use in a power turbine poses significant operational hur-

dles. First, the presence of hydrogen increases the reactivity of the mixture compared to conventional natural gas fuel. Consequently, several safety issues need to be considered. Second, since hydrogen is lighter, a larger volume of gas needs to be introduced into the combustor to generate the same thermal capacity. This requires alteration of the combustor design itself. The result of these two issues is the need to understand possible failure modes thoroughly so that the turbines could be operated safely and efficiently.

1.2   Flashback in syngas based turbines

Stationary gas turbines for power generation operate in the premixed mode, where fuel and air are mixed in a mixing chamber before being introduced into the combustor that contains the main reaction zone. This premixed combustion, when operated under fuel-lean conditions with excess air leads to lower operating temperatures and reduced production of NOx. In fact, aircraft engines that use direct fuel injection produce nearly an order of magnitude higher NOx concentration than the premixed ground-based turbines. Of course, this reduction in emissions comes at the cost of stability. Premixed combustors are notoriously prone to instabilities, including thermoacoustic oscillations, and a more catastrophic process termed flashback. In this latter process, the main flame in the combustor moves upstream into the mixing chamber towards the inlet nozzles. Since the mixing chamber is not typically designed to hold high temperature gases, this flashback could lead to combustor failure.

In natural gas burning power turbines, the combustors are optimized such that flashback could be detected early and preventive measures taken using inflow modulation or other active actuation strategies. Syngas combus-

tion changes the flashback process in a fundamental way that such actuation strategies are not sufficient. To understand this, it is important to note that flashback could occur through many different modes [11]. In conventional fuel combustors, the main mode of flashback is through vortex breakdown. Here, the swirling flow in the combustor generates a low velocity zone in which the premixed flame could propagate upstream since the burning velocity is faster than the local gas velocity. In syngas combustion, the main mode of flashback is through the boundary layers [10].

Boundary layers are thin fluid layers near solid boundaries that contain low momentum fluid due to the no-slip condition on the solid boundary. Figure 1.1 shows a schematic of a premixed flame propagating against the boundary layer. Note that the burning velocity of the fresh gases are determined primarily by the reactivity of the fuel and the turbulent modulation of the flame front. In the region close to the wall, the flame still encountered fresh gases but with lower momentum/velocity. Consequently, it is able to propagate upstream relative to the flame front away from the wall. Prior studies [10, 18] have shown that once this process is initiated, the velocity field upstream of the flame changes to accommodate a propagating flame, thereby enhancing the process. This interaction between the boundary layer (nominally turbulent) and the flame front is of fundamental importance in the design and operation of syngas-based combustors.

1.3   Motivation and objectives

Based on the discussion in the previous section, it is clear that boundary layer flashback (BLF) is an important process in syngas-based combustors. To aid design, predictive computational tools are very helpful. However, the

3
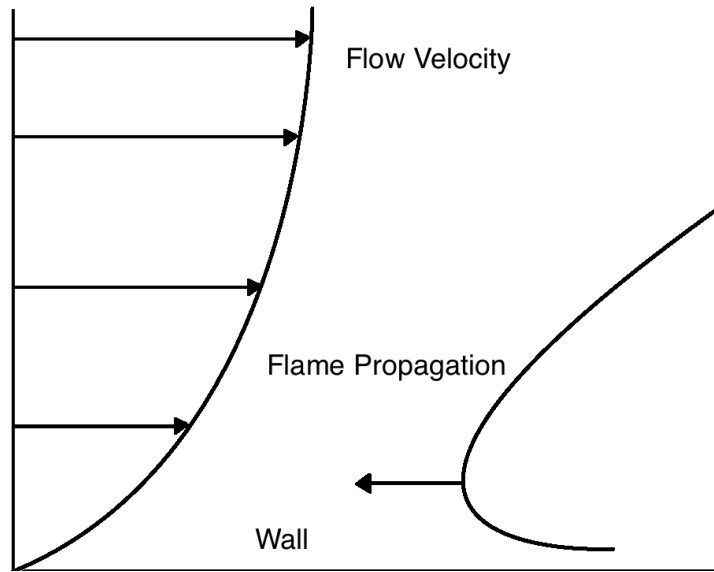
Figure 1.1: Schematic of the BLF process.

development of these tools are hindered by two issues. First, although there has been significant work in the simulation of flame propagation through turbulent flows, the application to propagation in boundary layers is relatively sparse. Second, gas turbine combustors involve very complex geometries (as do most practical systems). Hence, even if computational models are developed for flame-wall interactions, their transition into useful simulation tools is not straightforward. The objective of this work is to address both these issues to a limited extent, within the scope of a master's thesis.

After describing the mathematical formulation (Chapter 2) used for the simulations described, the rest of the thesis is laid out following specific objectives:

- Understand flame-boundary layer interaction (Chapter 3): To address

4

this issue, a collaborative effort with Sandia National Laboratories and the group of Dr. Jackie Chen is pursued. By using a high-resolution direct numerical simulation (DNS) database of flame flashback in a channel, the specific modeling issues for this process are analyzed. In particular, a large eddy simulation (LES) approach is followed. The predictive capability of LES is analyzed by simulating the DNS configuration with conventional premixed flame models. The ability to capture near-wall flame behavior is discussed.

- Low-Mach number solver for complex geometries(Chapter 4): In order to develop general purpose computational tools, a robust numerical implementation is developed here. One of the activities pursued in Prof. Raman's research group is the use of OpenFOAM [25] open source software to develop reliable computational tools for full scale simulation of combustors. However, currently available numerical algorithms are not consistent for reacting flows and do not provide robustness. Here, a second-order projection-based solver for collocated schemes is implemented and tested using method of manufactured solution (MMS).

Chapter 2

Mathematical Formulation

In this work, the turbulent flame propagation is described using the large eddy simulation (LES) framework. In the following sections, the governing equations and the models used to close the system are described.

2.1 Governing equations

The fluid system is described using conservation equations for mass, momentum, and energy. In addition, a set of species conservation equations are used to describe the chemical transformation that generate the flame structure. These governing equations are given by

$$\frac{\partial \rho}{\partial t} + \nabla \cdot (\rho \mathbf{u}) = 0, \tag{2.1}$$

where $\rho(\mathbf{x}, t)$ is the gas phase density and $\mathbf{u}(\mathbf{x}, t)$ is the velocity vector.

$$\frac{\rho \mathbf{u}}{\partial t} + \nabla \cdot (\rho \mathbf{u} \mathbf{u}) = -\nabla p + \nabla \cdot (2\mu(\mathbf{S} - \frac{1}{3}\mathbf{I}\nabla \cdot \mathbf{u})), \tag{2.2}$$

where p is the pressure, μ is the viscosity, and I is the Kronecker delta function expressed as a vector. In addition, transport equations for a set of species that describe the thermochemical composition vector need to be solved.

$$\frac{\partial \rho \boldsymbol{\phi}}{\partial t} + \nabla \cdot (\rho \mathbf{u} \boldsymbol{\phi}) = \nabla \cdot (\rho D \nabla \boldsymbol{\phi}) + \dot{\omega}(\boldsymbol{\phi}), \tag{2.3}$$

6

where D is the diffusivity (assumed to be equal for all species for the sake of simplicity here), and $\dot{\omega}$ is the chemical source term vector that is a function of the thermochemical composition vector. In general, it is common to express enthalpy or temperature as part of this vector, in which case the diffusivity is changed to account for differences in the enthalpy/temperature transport equation. For our purposes, we will not provide this distinction. Note that the LES model described below will dispense with the energy equation altogether due to the low-Mach number characteristic of the flow.

2.2   Filtered equations for LES

In general, the governing equations in the previous section cannot be solved directly for high Reynolds number flows. This is due to the fact that an Eulerian solution on a discrete grid will require grid-point separation comparable to the smallest flow features in the system, while the total dimension of the grid will be that of the flow geometry itself. The ratio of the geometrical size to the smallest required grid-separation scales as nearly a linear function of Reynolds number $(\mathrm{Re}^{3/4})$. Consequently, for realistic applications, the computational cost will be intractable. Note that this does not consider the added burden of evolving the species compositions, which will increase the cost easily by one to two orders of magnitude. One way to overcome this computational burden is through averaging [44]. There are two kinds of averaging possible - ensemble averaging leading to Reynolds-averaged Navier Stokes (RANS) approach or spatial averaging leading to the LES framework. The RANS approach, although mathematically elegant, removes much of the information about the turbulent flow and instead requires detailed models for these processes based on lower-order statistical quantities. Consequently, this

approach is falling out of favor compared to the LES approach.

In the LES framework, the governing equations (Eq. 2.2 - Eq. 2.3) are filtered using a spatial filtering operation defined as follows.

$$\overline{Q}(\mathbf{x}, t) = \int Q(\mathbf{y}, t) G(\mathbf{x}, \mathbf{y}) d\mathbf{y}, \tag{2.4}$$

where $\overline{Q}$ is the filtered field corresponding to Q, and G is a spatial filtering kernel. For variable density flows, the Favre-filtered field is defined as follows:

$$\overline{\rho}(\mathbf{x}, t) = \int \rho(\mathbf{y}, t) G(\mathbf{x}, \mathbf{y}) d\mathbf{y}, \tag{2.5}$$

$$\widetilde{Q} = \frac{1}{\overline{\rho}} \int \rho Q G(\mathbf{x}, \mathbf{y}) d\mathbf{y}, \tag{2.6}$$

where $\widetilde{(\cdot)}$ denotes the Favre-filtered variable. This filtering operation is applied directly to the governing equations to yield the filtered equations:

$$\frac{\overline{\rho}\widetilde{\mathbf{u}}}{\partial t} + \nabla \cdot (\overline{\rho}\widetilde{\mathbf{u}}\widetilde{\mathbf{u}}) = -\nabla \overline{p} + \nabla \cdot (2\overline{\mu}(\widetilde{\mathbf{S}} - \frac{1}{3}\mathbf{I}\nabla \cdot \widetilde{\mathbf{u}})) + \Im_u, \tag{2.7}$$

$$\frac{\partial \overline{\rho}\widetilde{\phi}}{\partial t} + \nabla \cdot (\overline{\rho}\widetilde{\mathbf{u}}\widetilde{\phi}) = \nabla \cdot (\overline{\rho}\widetilde{D}\nabla\widetilde{\phi}) + \Im_\phi + \overline{\dot{\omega}(\phi)}, \tag{2.8}$$

where $\widetilde{\mathbf{S}}$ is the strain rate tensor written in terms of Favre-filtered velocities. Two closure terms are introduced in the momentum and scalar equation to account for the subgrid scales. More precisely, $\Im_u = \nabla \cdot (\overline{\rho}\widetilde{\mathbf{u}}\widetilde{\mathbf{u}}) - \overline{\nabla \cdot (\rho \mathbf{u} \mathbf{u})}$, and $\Im_\phi = \nabla \cdot (\overline{\rho}\widetilde{\mathbf{u}}\widetilde{\phi}) - \overline{\nabla \cdot (\rho \mathbf{u} \phi)}$. These closure terms are respectively modeled with an additional eddy viscosity and eddy diffusivity using a dynamic Smagorinsky procedure [17].

The last term in the filtered species equation is the chemical source term which also appears filtered. In the spatial averaging context, this defines the

volume averaged chemical source term within a filter volume. It is important to note that the chemical source term is highly non-linear and will be active only in thin regions of the flow regardless of the nature of the system. In premixed combustion, the thickness of this reaction zone will be compared to the laminar flame thickness, while in diffusion flames the thickness will be of the order of the dissipation structures. Consequently, this term is dominated by high values in thin filaments that are typically much smaller than the filter volume. In addition, due to the high nonlinearity, the chemical source term evaluated based on the filtered species concentration will not be close to the filtered chemical source term. This disconnect is the essence of combustion modeling. The close of the chemical source term constitutes the turbulence-chemistry closure.

2.3   Combustion modeling

In general, the closure for the chemical source term could be based on one of two approaches: 1) A flame structure approach where the spatial structure of the flame is imposed to replicate a canonical flame configuration or 2) a statistical approach where the subfilter closure is treated as a probabilistic formulation. The first approach leads to flamelet-based closures [15, 23, 24, 26, 27, 37, 42], while the latter approach is exemplified by the probability density function [15, 43–45] and conditional moment closure [3, 16, 29]. In this work, the flamelet approach is used. This is mainly for two reasons: 1) The flamelet approach is computationally inexpensive and provides an excellent description of the flame structure, which in certain flow regimes is an accurate reproduction of flame behavior, and 2) the flamelet approach is widely used with LES and an analysis of its usefulness in predicting flashback will be of interest to the
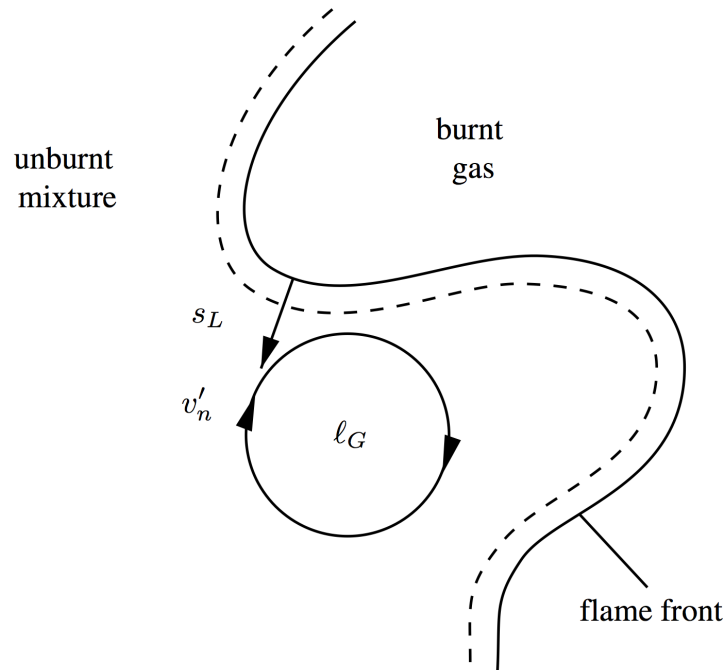
Figure 2.1: Premixed flame front structure from [38].

combustion modeling community.

For a premixed flame, the internal structure of the flame is represented by two regions [38], as illustrated in Fig. 2.1 :

- Reaction layer, where the key chemical reactions occur leading to energy release. This layer is usually an order of magnitude smaller than the defined flame thickness that encompasses the entire spatial variation due to the presence of the flame.

- Preheat zone, which is the region immediately upstream of the reaction layer where the chain branching reactions are initialized.

In the laminar flamelet approach, it is assumed that even in a turbulent flame the underlying flame structure is similar to that found in a freely propagating premixed flame under laminar flow conditions. This structure will be identical to the illustration above. Moreover, the effect of turbulence is to merely wrinkle the flame front so that the flame surface area is increased. Since the burning rate is directly proportional to this surface area, the combustion process is accelerated by the presence of turbulence. However, the smallest turbulence structures is still much larger than the preheat zone thickness so that the spatial structure of the flame remains undisturbed. Of course, as the Reynolds number increases (for a given geometry), the turbulence structures become increasingly smaller and at some point the preheat zone and maybe even the reaction zone is disturbed (stirred) by the flow field. In this case, flame quenching is possible. The different regimes of combustion could then be conveniently plotted in a regime diagram, as shown in Fig. 2.2 [6, 38].

As a closure model, the flamelet assumption then leads to the following simplification. A freely propagating flame is first simulated to provide the spatial structure of a one-dimensional flame. From this flame, the thermochemical composition vector is mapped using a tracking variable, which is termed progress variable for premixed flames. Essentially, given the progress variable it is then possible to determine the entire thermochemical state of the system. Under these assumptions, the entire set of species transport equations in Eq. 2.3 could be replaced by the transport equation for progress variable, which is given as follows:

$$\frac{\partial \overline{\rho \widetilde{c}}}{\partial t} + \nabla \cdot (\overline{\rho} \widetilde{\mathbf{u}} \widetilde{c}) = \nabla \cdot (\overline{\rho} \widetilde{D} \nabla \widetilde{c}) + \Im_c + \overline{\dot{\omega}_c}, \qquad (2.9)$$

where $\dot{\omega}_c$ is the chemical source term for the progress variable. In prac-
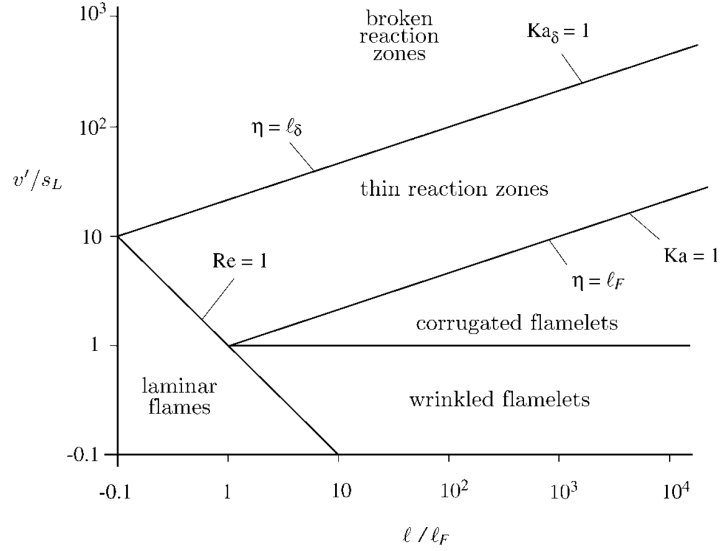
Figure 2.2: Regime diagram for premixed turbulent combustion from [38].

tical applications, this progress variable is chosen to be a monotonic descriptor that has the same spatial support as the flame itself. This ensures that the mapping is not extremely skewed and minimize error in the description of the thermochemical state. In this work, the fuel mass fraction is used as the progress variable.

In conclusion, the LES equations to be solved are filtered momentum transport equation (Eq. 2.7) and the filtered progress variable transport equation (Eq. 2.9). Following the low-Mach number approximation, the filtered mass conservation equation is ensured through the value of the fluctuating pressure which has no impact on the density. The density, viscosity and other chemical variables will be determined only based on a precomputed chemistry mapping relating them to the filtered progress variable value.

Chapter 3

Channel flashback

The goal of this chapter is to understand the capabilities of LES for modeling boundary layer flashback. More precisely, the impact of flame front resolution and combustion model on the boundary layer flashback process will be studied. The analysis is based on both *a priori* and *a posteriori* analysis of a direct numerical simulation (DNS) of channel flashback conducted by Gruber et al. [18].

After describing brief background of studies carried on it, the DNS results are presented. The LES simulations are then described, and the implementation of the investigated combustion models is detailed. A baseline combustion model is then used on several grid sizes to characterize the influence of flame front resolution. Local and macroscopic differences between LES and DNS are then analyzed to formulate modeling requirements for boundary layer flashback with LES.

3.1 Modeling objectives

Theoretical studies in laminar flames [31–33] have identified a critical near-wall velocity gradient necessary to arrest flashback. This relation correlates the burning velocity at the leading edge of the flame, the distance of this edge from the wall, and the velocity gradient at the wall. In general, a tur-

bulent boundary layer exhibits a higher critical velocity gradient as compared to a laminar boundary layer, which could be the result of a reduced distance to the wall or an increased burning velocity due to the core turbulent flow [10]. Computational studies mainly focused on laminar boundary layer flashback [31–33], with increasing complexity of the underlying flow description. Recently, Gruber et al. [18] conducted the first DNS of flame flashback in a three-dimensional channel flow using detailed chemical kinetics. The simulation indicates that density changes associated with the flame strongly influence the propagation mechanism. Also, small reverse flow regions in front of the flame actively accelerate it.

Predictive models that could capture the onset of flashback would be indispensable in gas turbine design. Due to the inherent transient nature of LES, it is seen as a promising tool for computationally describing flame flashback. The goal here is to assess the reliability of LES for such flows. In particular, we want to understand the modeling requirements for predicting flashback in confined geometries. Since LES resolves only the large scales, and the flame/boundary layer interaction occurs exclusively at the small scales, subfilter models should be able to handle the impact of density changes on flame and fluid propagation. In the simulations of vortex breakdown based flashback [48, 50, 51], it has been found that existing models reproduce flashback with reasonable accuracy, but unphysical near-wall flame propagation could be introduced by the nature of the chemical source term closures used [50]. In these studies, flashback occurs primarily in the core of the flow, away from the walls, and subfilter closures based on the assumption of local equilibrium [36, 47] could be invoked without introducing appreciable errors. In boundary layer flashback, the balance of production and dissipation in the

near wall region needs to be assessed in order to determine the accuracy of equilibrium-based subfilter models.

This discussion leads to the following question: What are the features of the flow that need to be reproduced for an LES-based model to predict flashback? To understand this question, we utilize a posteriori simulations of a high-fidelity DNS configuration studied by Gruber et al. [18]. The study assesses the key physical characteristics that need to be represented in order to reproduce flashback using LES computations. A suite of LES computations is used to understand the key interactions between the flame and flow field. Statistical quantities describing the structure of the flame front are used to evaluate LES performances.

3.2   DNS flow configuration

Figure 3.1 shows a schematic of the flow configuration used in both the DNS and LES computations. The domain measures $0.06\,\mathrm{m} \times 0.012\,\mathrm{m} \times 0.036\,\mathrm{m}$ in the streamwise, wall-normal, and spanwise directions, respectively. In the DNS computation, a $2400 \times 480 \times 1440$ point computational grid is used. The grid is uniform in all directions, giving a spacing of $\Delta_x = 2.5 \times 10^{-5}\,\mathrm{m}$. Premixed hydrogen-air mixture was fed through the inlet with a bulk velocity of $20\,\mathrm{m/s}$ leading to a Reynolds number of 3200. The equivalence ratio of the mixture was 0.55, and the inflow temperature was set at $750\,\mathrm{K}$. The flow field was allowed to develop inside the channel for a finite time before the flame front was initialized at X = $0.045\,\mathrm{m}$ by superimposing a 1D laminar flame profile. The velocity field was adjusted to account for the change in density. Hydrogen combustion was simulated using a 9-species 19-step reaction mechanism [34]. The inflow to the DNS configuration was a

15
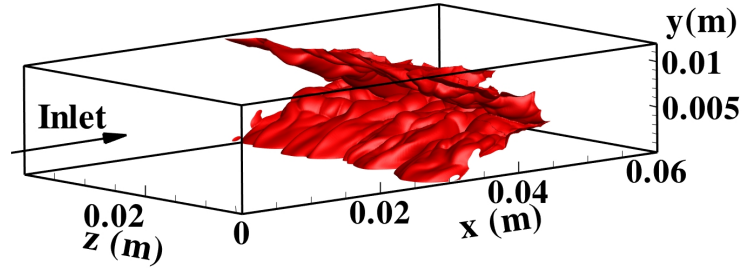
Figure 3.1: Channel flow configuration, where X is the streamwise direction, Y is the wall-normal direction, and Z is the spanwise direction. Also shown, is the DNS instantaneous isocontour of $\widetilde{c} = 0.7$ filetered with a Gaussian filter of size $\Delta = 8\Delta_{x,DNS}$ for t = 7.880e-04 s, measured from the time of initialization.

temporally evolving turbulent velocity field extracted from an auxiliary inert DNS with a bulk velocity of 20 m/s.

Figure 3.2 shows instantaneous flame front contours at different times. As expected the flame progresses through the low velocity near-wall region, with the higher velocity near the channel centerline pushing the flame downstream. Not shown here, in the initial stages the flame is pushed downstream from the initialization point before flashback takes hold. The flame has a sinusoidal front near the walls (Fig. 3.1), indicating regions of positive curvature that are accelerated as the flame propagates upstream. The DNS computation was run for a longer time but the data used in this work corresponds to the leading edge of the flame being displaced only by about 5 mm. However, flame propagation in this region is beyond the initial transient state and the upstream propagation velocity is roughly uniform.

The stream wise velocity component (Fig. 3.2) shows the acceleration of the flow behind the flame front. The flame front acts as a blockage for the flow which diverts the near-wall fluid toward the centerline causing an acceleration

16
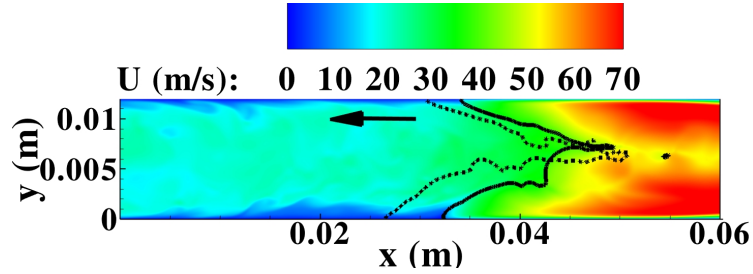
Figure 3.2: Instantaneous DNS contour of streamwise velocity component at t = 0.788 ms. The solid line represents the flame front isocontour based on c = 0.7 at that time instant, while the dashed line is the flame front at t = 1.44 ms. The arrow indicates the direction of flashback.

before reaching the flame. The gas expansion causes a second acceleration that make the velocity reach values close to 70 m/s. Figure 3.2 also shows the flame front at the earliest and latest time instances that encompass the entirety of the DNS data used in this work. Note that in this duration, the flame front motion is almost uniform allowing for temporal averaging in collecting statistics.

3.3 LES computations

The LES approach uses a grid-based filtering technique. As described in Chapter 2, the flame evolution is described using a flamelet approach, where a transport equation for the Favre-filtered progress variable is solved along with the filtered continuity and momentum equations. A low-Mach number technique based on a pressure-projection algorithm is used [1, 39]. In the filtered progress variable equation given by Eq.2.9, it was required to access the filtered diffusivity of the progress variable. Since only the unfiltered diffusivity is accessible, the filtered transport equation for progress variable is written as

17

$$\frac{\partial \overline{\rho} \widetilde{c}}{\partial t} + \nabla \cdot (\overline{\rho} \widetilde{\mathbf{u}} \widetilde{c}) = \nabla \cdot (\alpha(\widetilde{c}, \Delta_{LES}) \overline{\rho} D \nabla \widetilde{c}) + \Im_c + \overline{\dot{\omega}}, \qquad (3.1)$$

where α is a model for the correlation between the diffusivity and the scalar gradient, Δ_{LES} is the LES filterwidth and $\overline{\dot{\omega}}$ is the filtered chemical source term. The second term on the right hand side is the subfilter scalar flux term. In general, there are many different models available for closing these terms [5, 7, 14, 19, 49]. In this study, three different models will be tested and are described in Section 3.3.2.

3.3.1 Flow field resolution

The mesh sizes used in the domain are uniform and equal. Grid sizes ranging from 16 to 4 times the DNS resolution are used. This implies that the largest mesh size used in the domain is 0.4 mm. An analysis of the DNS flow also showed that the Kolmogorov length scale η in the core flow was equal to 0.25 mm. As a consequence, the mesh size is sufficiently small to consider that the flame wrinkling fully resolved. As pointed out by [13], with increasing computational power, this regime where turbulence is well resolved has become the norm. Consequently, representing laminar flame propagation accurately with minimal computational cost becomes the critical step. The flow equations contain unresolved stress terms, which are closed here using a dynamic Smagorinksy model [17]. The LES equations are solved using a second-order accurate time-stepping scheme [8, 40]. The convection terms in the momentum equations are discretized using an energy conserving second order scheme, while the scalar convection terms were solved using the B-QUICK scheme [20].

18

3.3.2 Progress variable based combustion models

All models implemented with this configuration use the progress variable approach introduced in Sec. 3.3. The evolution of the flame is described by solving for the progress variable, but closures for the chemical source term, the molecular diffusivity term (due to the change in diffusivity with temperature), and the subfilter scalar flux term are needed. In this work, the progress variable is defined as

$$c = \frac{Y_{H_2} - Y_{H_2,u}}{Y_{H_2,b} - Y_{H_2,u}}, \tag{3.2}$$

where Y_{H_2} is the local mass fraction of H_2, $Y_{H_2,u}$ is the mass fraction of H_2 is the fresh gases and $Y_{H_2,b}$ is the mass fraction of H_2 is the burnt gases (close to zero for a lean mixture). With this definition, the progress variables takes values between 0 and 1, with the null values on the unburnt side and 1 value on the burnt side of the reaction.

3.3.2.1 Direct flamelet model (DF)

In the DF model, The 1-D laminar premixed solution is directly mapped to filtered progress variable space, and no convolution rules are used to transform the raw progress variable to a filtered value. All unclosed terms are determined by first computing a mapping between the progress variable chosen and the terms needed to be mapped. To compute this mapping, a steady 1D laminar premixed flamelet simulation with detailed chemistry is performed using the Flamemaster code [41].This model represents the crudest approximation of the flame front. Here α is set to 1, and the subfilter flux is modeled using gradient-diffusion hypothesis [12].

19

3.3.2.2 Filtered tabulated chemistry for LES (F-TACLES)

In the F-TACLES approach, the 1D laminar flame solution is filtered using an explicit Gaussian filter, which is different from the LES filter. The resulting filtered progress variable is used as the mapping variable. In this approach, α is specifically constructed from the flame solution. As described by [2], the three terms on the right hand side of Eq. 3.1 can be directly obtained from this filtering procedure. The direct use of the flamelet solution or the filtered solution faces a computational hurdle. In LES, the scales that are resolved are comparable to the smallest grid size. However, numerical errors scale with wavenumber, which implies that scales closest to the smallest resolved scales incur the largest error. Hence, the solution of progress variable, which exhibits strong jumps at small scales near the flame front, is subject to considerable numerical error. One solution to this problem is to artificially thicken the flame when constructing the filtered mapping variable by filtering the 1D flamelet solution with a filter width larger than the LES filter width. Note that the DF model presents the other end of the spectrum where the flame is under-resolved by the LES mesh. Figure 3.3 shows the different closed terms plotted as a function of the filtered progress variable.

3.3.2.3 Algebraic flame surface density model (AFSD)

The AFSD model is based on a flame surface density approach, and does not explicitly rely on the flamelet assumption. The diffusion and chemical source terms are modeled as

$$\nabla \cdot (\alpha(\widetilde{c}, \Delta)\overline{\rho}D\nabla\widetilde{c}) + \overline{\dot{\omega}} = \rho_u S_l \Sigma, \tag{3.3}$$

where ρ_u, S_l and Σ are the unburnt density, laminar burning velocity, respectively. Σ is the flame surface density that needs to be specified. This quantity

20
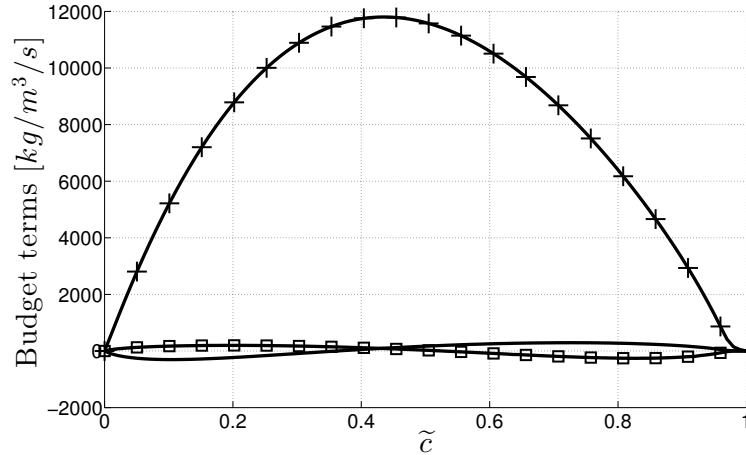
Figure 3.3: Filtered source terms obtained from the F-TACLES procedure for filter width $8\Delta_{x,DNS}$: $\frac{\partial}{\partial x_i}\alpha(\widetilde{c},\Delta)\overline{\rho}D\frac{\partial\widetilde{c}}{\partial x_i}$ (solid line), $-\nabla\cdot\overline{\rho}\left(\widetilde{u_i c}-\widetilde{u}_i\widetilde{c}\right)$ (solid line with squares), and $\overline{\rho}\widetilde{\dot{\omega}}$ (solid line with crosses). Y-axis has units of $kg.m^{-3}s^{-1}$.

obtained with an algebraic model [5] that relates the subfilter variance of progress variable to the flame surface density.

$$\Sigma = 4\beta\frac{\overline{c}(1-\overline{c})}{\Delta}, \tag{3.4}$$

with β being a tunable coefficient and Δ the LES filterwidth. Here, the value of β is chosen such that certain properties of the DNS are reproduced. This is further discussed in Sec. 3.5.3. The subfilter flux term is prescribed using a gradient-diffusion hypothesis.

3.4 Implementation of combustion models

As described in the previous sections, the numerical implementation of the progress variable based models requires specific choices regarding filter width and model parameters. For the DF model, the implementation is

entirely defined by the closures terms directly obtained from the steady 1D laminar flame solution, and no more implementation considerations are required. However, for the F-TACLES model, the flamelet filterwidth needs to be defined prior to any simulation. For the AFSD model, the tunable parameter β also needs to be determined a priori. Here, an *a priori* analysis is used to determine these values. The F-TACLES filterwidth is chosen based on a 1D analysis of the flame propagation, while the AFSD tunable parameter β is determined using integral analysis of the progress variable source term.

3.4.1 1D analysis for F-TACLES

A 1D simulation with the same mass flow rate as the channel flashback case is performed. The goal is to use the F-TACLES approach to obtain the correct laminar propagation speed. The 1D progress variable equation (Eq. 3.1) is solved using the F-TACLES source terms are described before. The main impact of filtering the flame front using a larger filter size than the mesh size is to increase the flame thickness for an constant number of grid points.This is shown in Fig. 3.4 and Fig. 3.5 .

Here, the laminar flame thickness is equal to 0.18 mm while the smallest mesh size used is equal to 0.1 mm. It is expected that a higher resolution of the flame front can have an impact on the laminar flame speed error retrieved form the 1D analysis. It is also expected the the laminar flame speed is mainly driven by the progress variable source term integral in the 1D domain. Figure 3.5 shows a comparison between discretized and the ideal progress variable source term for two different Δ_F and the same Δ_x.

It is can be immediately seen that having a higher mesh resolution of the progress variable source terms leads to better integrated value for the
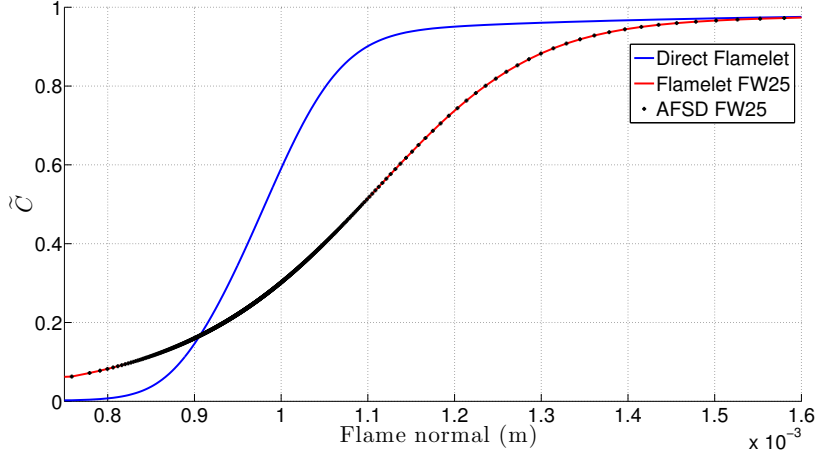
Figure 3.4: Influence of filtering on the progress variable spatial distribution extracted from the 1D laminar solution.

progress variable source term profile in discretized space. As a result, the observed flame speed in the 1D laminar simulation is closer to the theoretical laminar flame speed. Figure 3.6 shows the evolution of the flame front position in the domain. After a transient time, the slope of the curves reach a steady value from which is extracted as the observed laminar flame speed.

When using $\Delta_F = 25\Delta_{x,DNS}$, the observed laminar flame speed is $5 - 10\%$ higher than the theoretical laminar flame speed. For $\Delta_F = 8\Delta_{x,DNS}$, the observed laminar flame speed overestimated the theoretical value by up to 70%. Increasing even more the flamelet filtersize does not lead to appreciable differences in terms of observed flame speed (not shown here). All F-TACLES and AFSD simulations were conducted with a filtersize $\Delta_F = 25\Delta_{x,DNS}$.
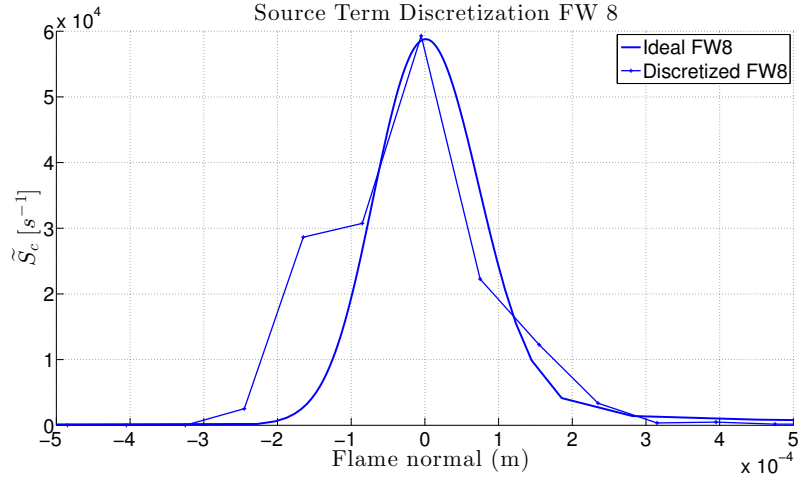
(a) Figure A : $\Delta_F = 8\Delta_{x,DNS}$.
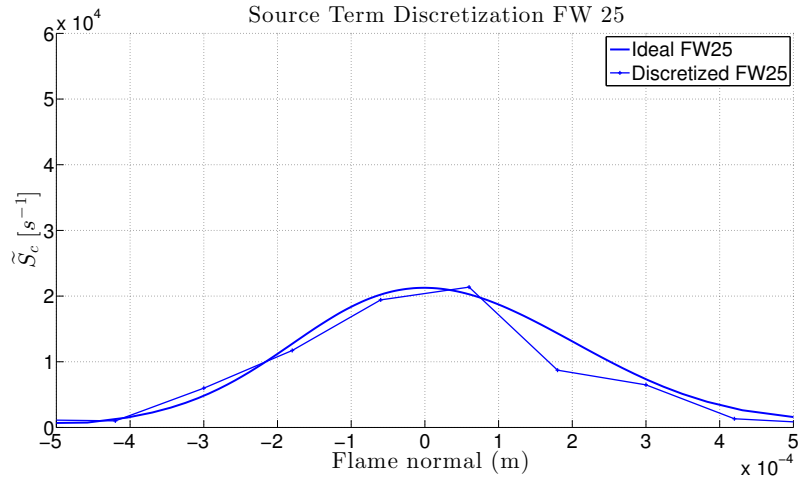
(b) Figure B : $\Delta_F = 25\Delta_{x,DNS}$.

Figure 3.5: Discretization error observed for the tabulated progress variable source term with filter size $\Delta_F = 8\Delta_{x,DNS}$ (Figure A) and $\Delta_F = 25\Delta_{x,DNS}$ (Figure B).
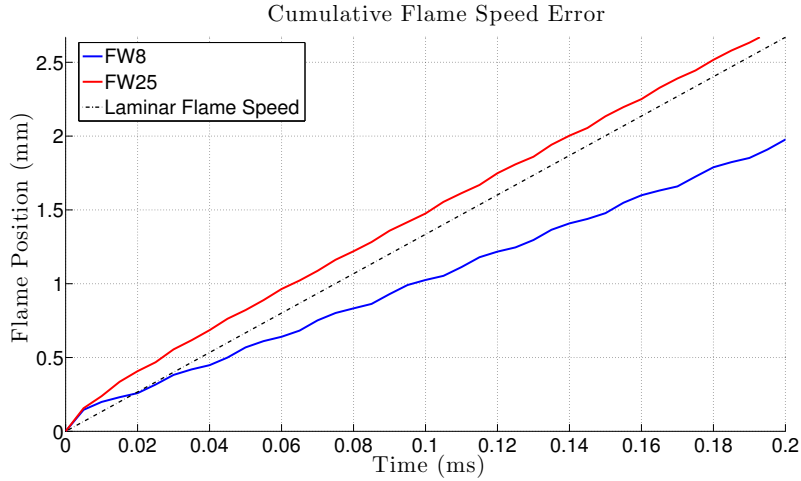
Figure 3.6: 1D flame propagation using tabulated chemistry and filtered with a Gaussian filter. (Blue line) $\Delta_F = 8\Delta_{x,DNS}$, (red line) $\Delta_F = 25\Delta_{x,DNS}$, (dashed line) theoretical 1D flame propagation.

3.4.2 Integral analysis for AFSD

As explained before, the AFSD model uses an algebraic closure formula for the diffusion and chemical source terms of the progress variable transport equation. This algebraic formula involves a tunable coefficient β that needs to be determined prior to a simulation. To do so, a similar analysis as for the F-TACLES model is performed to characterize the flame speed propagation with the integrated value of the closed progress variable source term. The targeted value for the integrated progress variable source term is the one obtained with an unfiltered 1D steady laminar analysis. With an iterative process, a value for β for each filter size Δ_F can then found. In the LES simulations, for a flamelet filter size $\Delta_F = 25\Delta_{x,DNS}$ a model coefficient $\beta = 0.827$ is chosen for the AFSD model based on this analysis.

3.5   Results and discussion

Two different groups of LES calculations are carried out. First, the effect of the combustion models is tested using the three models described in Sec. 3.3.2. Second, the effect of filter width is discussed. A third set of calculations where the LES is initialized using different initial conditions for the flow field was also carried out. For these calculations, a LES filterwidth $\Delta_{LES} = 16\Delta_{x,DNS}$ along with the F-TACLES model was used. There was no appreciable change in the flame front propagation for the different cases in this set. This implies that flame front propagation is the accumulated interaction with multiple eddies over resolved-scale time scale, and that variability in initial conditions are washed out by the short length-scale associated with eddies that affect the flame front. Before discussing the two sets of calculations, the baseline case is presented in detail to motivate the key parameters targeted in the flashback computations.

3.5.1   Baseline LES computation of flashback

The baseline case is based on the F-TACLES model with $\Delta_F = 25\Delta_{x,DNS}$. Figure 3.7 shows the LES-based isosurface of $\widetilde{c} = 0.7$ at the earliest and latest time for which corresponding DNS data is available.

Several qualitative similarities can be seen between the DNS and LES computations. At comparable times, the flame structures in both DNS and LES are very similar. The flow is diverted away from the walls by the flame-induced blockage, which causes an acceleration of the flow along the center. Gas expansion in the post-flame region further increases the flow rate. However, in the LES calculation at earlier time, the lack of a v-shaped flame prevents the centerline acceleration. Consequently, the post-flame velocities are

26
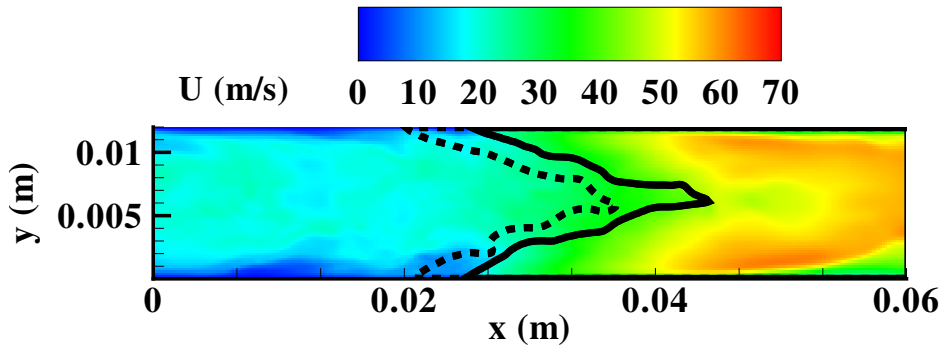
Figure 3.7: Instantaneous LES contour of streamwise velocity component at t = 0.8 ms. The solid line represents the flame front isocontour based on c = 0.7 at that time instant, while the dashed line is the flame front at t = 1.4 ms. The arrow indicates the direction of flashback.

much lower than that for DNS and are essentially the density-scaled turbulent channel flow velocities. At later times, as the flame front becomes similar to the DNS, the post-flame velocities are of the same order as DNS.

Figure 3.8 shows the three-dimensional isosurface of progress variable at a time comparable to that of the DNS in Fig. 3.1. It is seen that the DNS surface exhibits a wide range of scales (as expected) with smooth variations on the surface interspersed with short-lengthscale fluctuations in the streamwise location of the flame front. In addition, the positive curvature regions near the wall that tend to accelerate the flame are more pronounced with deeper troughs along the streamwise direction. Although the LES flame surface exhibits similar troughs, the depth of these features is considerably smaller. As a consequence, the spanwise variation in the flame front location in the near wall region is smaller compared to the DNS case. Figure 3.11 shows the PDF of the flame location in both DNS and LES computations, and illustrate the fluctuation of the flame front location in the streamwise direction about the

27
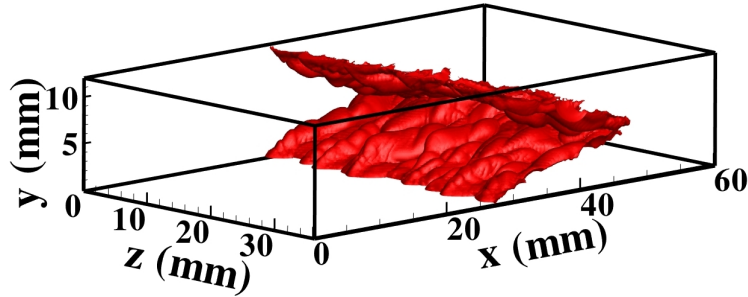
Figure 3.8: Instantaneous isocontour of $\tilde{c} = 0.7$ obtained from LES using a filterwidth of $8\Delta_{x,DNS}$.

spanwise-averaged flame front location. It is seen that the LES-based PDF roughly matches the near-Gaussian DNS-based PDF. However, the probability of large fluctuations is marginally lower than the DNS probability.

3.5.2 Quantitative parameters

To further understand the LES results, two quantitative parameters are introduced to describe the macroscopic flame structure and the flame propagation. The evolution of the distance between the leading and trailing edges of the flame is studied. For the purpose of this discussion, the leading edge is the first point along the x-axis in a single z-plane that contains a non-zero progress variable, while the trailing edge is the last grid point in the x-direction that contains a zero progress variable. This quantity, termed flame depth here, incorporates the cumulative effect of the core velocity on the propagation characteristics. Note that in the boundary layers where the flow field is nearly laminar, propagation is mainly at the laminar flame speed, while in the core flow, turbulent flame wrinkling will lead to turbulent-velocity based propagation. In the extreme case of the depth being zero, the difference between

28

Figure 3.9: Plot of spanwise averaged depth parameter as a function of time for DNS (circles) and LES with F-TACLES (solid line), FSD with $\beta = 0.2$ (dash-dotted line), and FSD with $\beta = 0.66$ (dashed line) at $\Delta_{LES} = 8\Delta_{x,DNS}$.

the core velocity and the turbulent propagation speed matches the difference between the laminar burning velocity and the boundary layer mean velocity.

Figure 3.9 shows the spanwise-averaged depth as a function of time. It is seen that for the baseline case (red line) this quantity increases with time but ultimately reaches a slowly varying stage after 0.5 ms. The depth in the DNS is steady in this time interval at roughly 0.015 m. The increase in LES is expected as the flame is wrinkled from its initial flat condition. But the continued growth indicates that a) the trailing edge of the flame is not able to propagate strongly against the high velocity near the centerline, and b) the streamwise velocity in the near-wall region ahead of the leading edge of flame is weaker than in DNS leading to faster flame propagation, relative to the center of the flame.The F-TACLES flame is the only solution that also seems to reach a slowly varying stationary state.

To analyze the flame propagation, a second quantitative parameter denoted as flashback velocity is introduced. This parameter is computed based on the evolution of the volume of burnt mixture in the domain. This is a global parameter that does not take into account the difference between walls and core flow. The flashback velocity is quantified as

$$U_{FLBK}(t) = \frac{1}{S_{Channel}} \iint_{S_{Channel}} s_T(x,y,z,t) - U(x,y,z,t) ds \qquad (3.5)$$

which can be approximated as

$$U_{FLBK}(t) = \frac{S_{Flame}(t)}{S_{Channel}} s_L - u_{BULK} \qquad (3.6)$$

This criteria is then a useful parameter to quantify how accurately is represented the flame wrinkling.

Figure 3.10 shows the flashback velocity variation in time for the models considered in this study. It can be seen that initially the flame is convected downstream (negative velocity) before flashback takes hold. But even then, the propagation velocity is lower than the DNS velocity. This explains the observation hat both flame fronts are at similar locations for the time-intervals considered even when starting from different initial locations. Note that for the baseline case, the flame velocity remains constant after a transient time, even though the flame depth increases. This means that while the flame is being stretched globally, the local flame wrinkling is decreased such that the global flame surface remains the same.
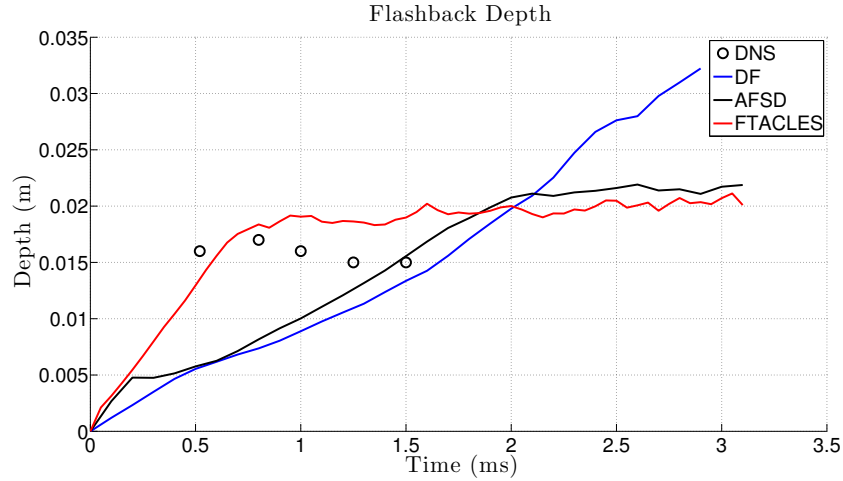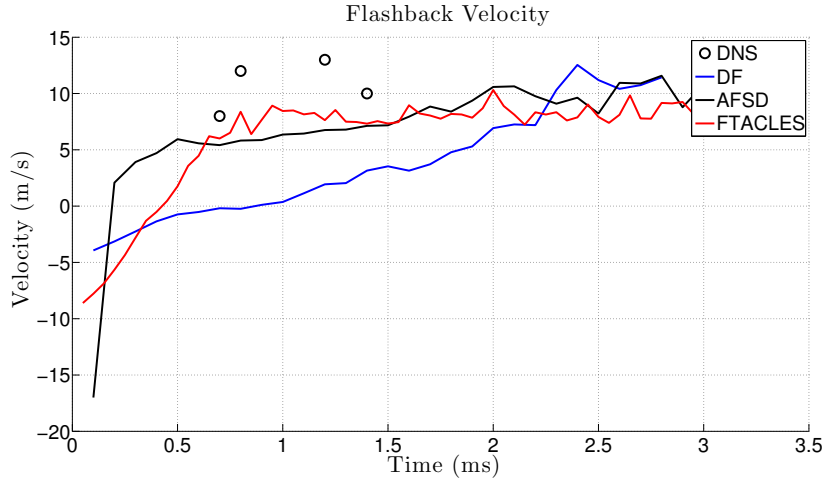
Figure 3.10: Plot of spanwise averaged velocity as a function of time for DNS (circles) and LES with F-TACLES (solid line), FSD with $\beta = 0.2$ (dash-dotted line), and FSD with $\beta = 0.66$ (dashed line) at $\Delta_{LES} = 8\Delta_{x,DNS}$.

3.5.3 Effect of flame model on propagation

To understand the role of the model in predicting the parameters of flashback defined in Sec. 3.5.2, the three different models described in Sec. 3.3.2 were used with $\Delta_x = 8\Delta_{x,DNS}$. The DF model produced very inaccurate results. It was in fact found that the flame propagation was very dependent on the scheme used for the scalar interpolation. The results for DF are shown in this section to emphasize the role of the resolution of the filtered flame front.

The F-TACLES (Fig. 3.7) model is accurate in representing flame propagation. Quantitatively, the depth parameter (Fig. 3.9) is accurately represented. However, it can be seen that the flame wrinkling is clearly underestimated compared to the DNS data. The post-flame velocities are of the same order as in the DNS. It can be also observed that the blockage effect induced by the flame (V-shape acceleration of the flow field) is underestimated compared

to DNS.

The AFSD model fails to accurately represent the mean flame shape. This is very likely due to the fact that diffusion is taken into account in the flame normal direction, but does not depend on the flame topology. As a result, the flame shape follows directly the velocity profile in the channel. The post-flame velocity also underestimates the DNS data by around 30%. As the flame propagates because the mean flow velocity peaks at the channel centerline, the DNS flame shape is progressively recovered (Fig. 3.13). Note also that as the flame shape is recovered, the post-flame velocity bridges the gap with the DNS post-flame velocity. As a result, the depth parameter (Fig. 3.9) is underestimated at the beginning but is predicted much better at later times. As the flame stretches with time, the DNS-based flashback velocity parameter gradually increases to nearly the value found from the F-TACLES model (Fig. 3.10).

3.5.4 Effect of LES grid on propagation

Three different grid sizes of 4, 8, and 16 times the DNS grid spacing were used. For all these computations, the F-TACLES model was used with a constant flamelet filter size $\Delta_F = 25\Delta_{x,DNS}$. In addition, the computational grid associated with each width was refined in the wall-normal direction to add twice the number of points in the low-velocity region. Grid clustering did not change the propagation speed nor the depth parameter as compared to the uniform mesh case for both filterwidths. This was surprising as better near-wall resolution should be expected to better represent the flashback process. This suggests that a minimum resolution is needed to reproduce flashback but additional resolution does not necessarily introduce any new physics capable of
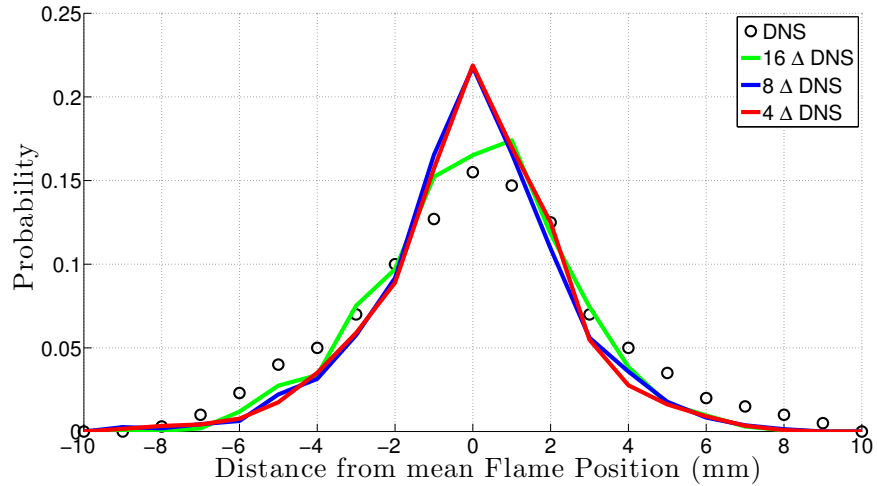
Figure 3.11: PDF of distance from the mean $\widetilde{c} = 0.7$ isocontour for DNS (circles) and LES with F-TACLES with $\Delta_F = 4\Delta_{x,DNS}$ (red line), F-TACLES with $\Delta_F = 8\Delta_{x,DNS}$ (blue line), F-TACLES with $\Delta_F = 16\Delta_{x,DNS}$ (green line).
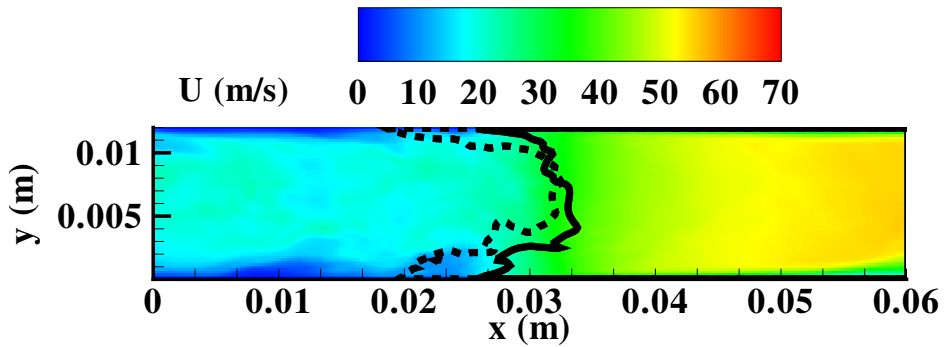
Figure 3.12: Instantaneous LES contour of streamwise velocity component at $t = 0.8\,\text{ms}$ for the AFSD model. The solid line represents the flame front isocontour based on $c = 0.7$ at that time instant, while the dashed line is the flame front at $t = 1.4\,\text{ms}$.
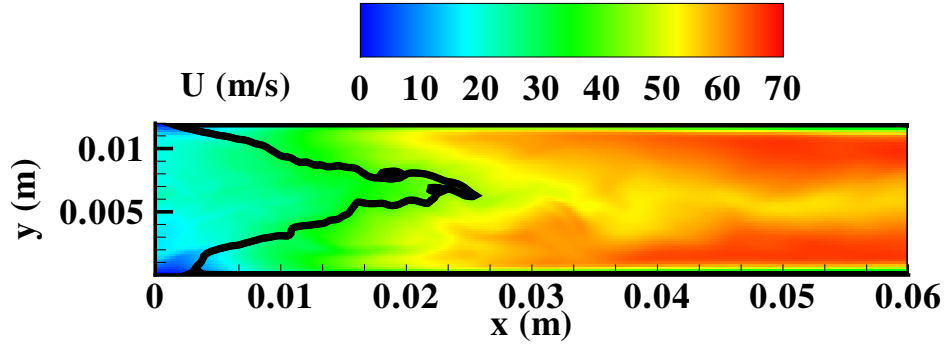
Figure 3.13: Instantaneous LES contour of streamwise velocity component at t = 3.0 ms for the AFSD model. The solid line represents the flame front isocontour based on c = 0.7 at that time instant.
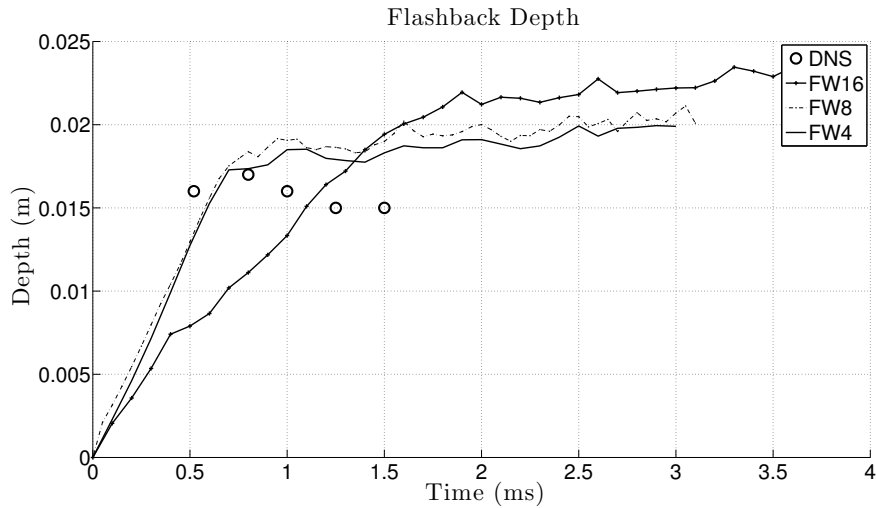
Figure 3.14: Plot of spanwise averaged depth parameter as a function of time for DNS (circles) and LES with F-TACLES with $\Delta_{LES} = 4\Delta_{x,DNS}$ (solid line), $\Delta_{LES} = 8\Delta_{x,DNS}$ (dashed line) and $\Delta_{LES} = 16\Delta_{x,DNS}$ (solid line with dots).
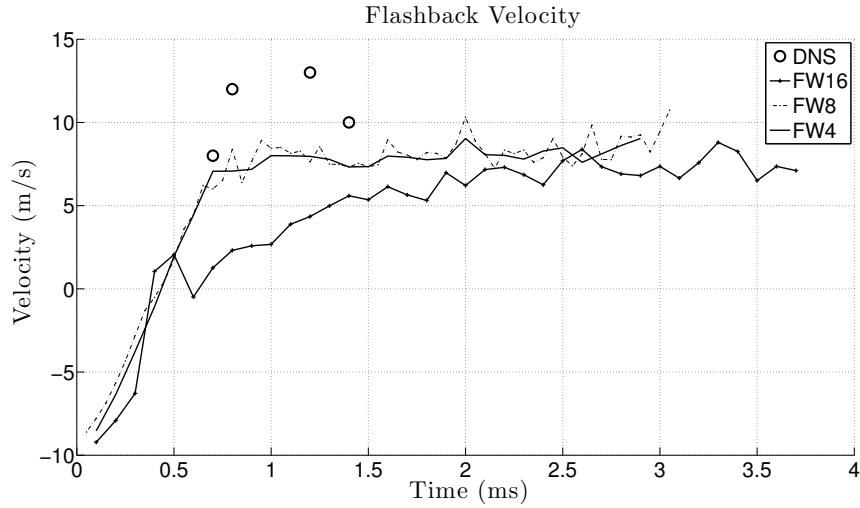
Figure 3.15: Plot of spanwise averaged velocity as a function of time for DNS (circles) and LES with F-TACLES with $\Delta_{LES} = 4\Delta_{x,DNS}$ (solid line), $\Delta_{LES} = 8\Delta_{x,DNS}$ (dashed line) and $\Delta_{LES} = 16\Delta_{x,DNS}$ (solid line with dots).

altering the flame dynamics. However, the change of filterwidth from $8\Delta_{x,DNS}$ to $16\Delta_{x,DNS}$ had a large effect on the transient flame evolution. Figure 3.14 shows the evolution of the depth parameter for the three filterwidths. It can be seen that not much difference can be observed between $4\Delta_{x,DNS}$ to $8\Delta_{x,DNS}$. For the coarsest mesh, the transient evolution of the flame depth is not accurately represented. However, the flame reaches a final flame depth close from the other reached by the finer simulations.

3.6 Conclusions

A suite of LES computations was used to understand the modeling of boundary layer flashback in relatively low Reynolds number but turbulent channel flow. The LES filterwidths were comparable to the smallest turbulence

length scales, which would imply that the momentum description is reasonably accurate in the LES calculations. The flame, on the other hand, was approximated as a thin front using different models. In this sense, the computations were designed to test the interaction of this thin-flame assumption with the near-fully resolved flow field. The computations found certain intriguing features. The baseline case at $\Delta_{LES} = 8\Delta_{x,DNS}$ produced a flame front that is comparable in statistics to that in the DNS. Using quantities such as the depth parameter and the PDF of front fluctuations, it was found that the LES computations are very accurate in predicting the structure of the turbulent flame front. However, there was a discrepancy in the propagation velocity of the flame front. In other words, a slowly moving LES flame front was able to produce the structures of a faster moving DNS front. The flamelet-based models produced lesser variability to simulation conditions, including the choice of other subfilter models. This is expected, given that the chemical source term is the predominant quantity in the progress variable transport equation as it can be seen in Fig. 3.3. It was found for the AFSD model that representing accurately the diffusion term was crucial to observe the characteristic flame blockage described by Gruber et. al. [18]. A similar behavior for the depth and flashback velocity parameter was observed with coarse F-TACLES model.

Even for the lowest resolution grids, flashback was still predicted, indicating that flame propagation through the boundary layers could be captured with minimal resolution. Interestingly, additional variations on these basic computations did not produce any changes to the flow. For instance, adding more points to the near-wall region did not change the depth or the velocity of propagation. Also, starting the calculation from different initial conditions led to almost no perceptible difference in these characteristics of the flame.

Based on these results, the requirements to capture the flashback process could be divided into three parts. First, there should be sufficient resolution near the wall to represent the actual V-shape of the flame, and at least approximately, the transition to a laminar flow. Combined with the density change across the flame, this creates a blockage to divert the flow towards the center. Second, the blockage-created centerline acceleration in the core of the channel is necessary to maintain the V-shape of the flame. Third, the combustion model should ensure that the core is not pushed downstream with the flow. In other words, the transition from a fully laminar to, possibly unresolved, wrinkled flame needs to be captured. However, the requirements for obtaining the correct propagation velocity seem to rely on additional physical model characteristic of the configuration, such as wall heat loss, differential diffusion or the impact of near-wall streaks.

Chapter 4

Implementation of a low-Mach number solver for complex geometries

In the previous chapter, the physics of boundary layer flashback was analyzed using a canonical flow configuration. In practical gas turbine combustors, the flame is stabilized using swirling inflow which requires complex geometric features. Consequently, the simulation of a full gas turbine combustor requires robust numerical techniques that could be applied to generalized computational grids. To transition the lessons learnt in the modeling chapter, we provide the second part of this work, which is the development of robust temporally accurate numerical solver for variable density flows.

The motivation behind this study is to develop open source technology that allows rapid transfer of research advances to industry. Based on our collaboration with Siemens Inc., the OpenFOAM open source package [25] was selected as the simulation platform. The low-Mach number solver is developed for this unstructured grid approach.

4.1   Solver development and reference solution

In our group, we have access to two different solvers: the OpenFOAM package discussed above and an energy conserving structured solver, NGA, developed at Stanford University by Prof. Pitsch and his graduate students [9].

The structured flow solver is only capable of solving canonical flow geometries and cannot handle complex features. However, the solver is highly accurate for evolving LES equations and has been used widely by a number of research groups on a variety of applications [4, 21, 22, 37]. Our objective in this work is to implement the algorithm in the NGA solver into the OpenFOAM package.

OpenFOAM and NGA differ in their implementation in a fundamental way. NGA uses staggered grid representation illustrated in Fig. 4.1, while the unstructured grid OpenFOAM solver uses a collocated mesh representation (Fig. 4.2). Similarly, the time-stepping in NGA also uses a staggered scheme, where the velocity is advanced based on half-steps. OpenFOAM, on the other hand, uses standard temporal discretizations based on previous time steps. With this discussion, the focus of this chapter is the development of the OpenFOAM based LES solver. The NGA code is referenced only to illustrate the differences between staggered and collocate mesh solvers, especially in the context of pressure solution.

4.2 Collocated mesh low-Mach number solver

For the sake of this discussion and without loss of generality, a 1D simulation domain is considered. Written with an implicit Euler time discretization, written between the time n and n+1, the governing discrete equations are then

$$\frac{\rho^{n+1}\phi^{n+1} - \rho^n\phi^n}{\Delta t} + \frac{1}{V_{cell}}\sum_f S_f\rho_f^{n+1}U_f^{n+1}\phi_f^{n+1} =$$

$$\frac{1}{V_{cell}}\sum_f S_f(\rho D)_f\frac{d\phi}{dx}_f + \dot{\omega}(\phi^n), \quad (4.1)$$
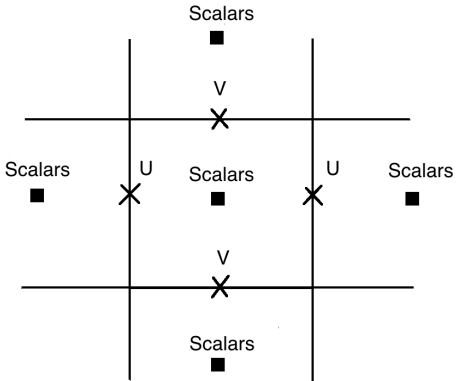
39

Figure 4.1: Illustration of the staggered grid used in NGA. p denotes pressure and ρ denotes density.
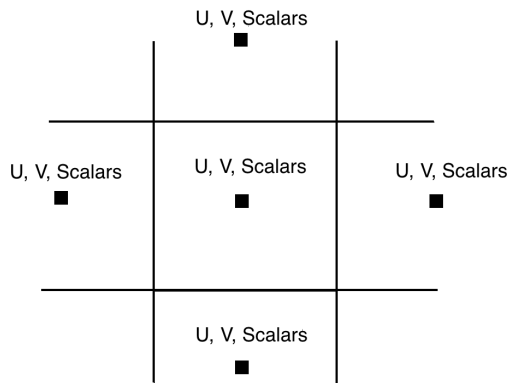

Figure 4.2: Illustration of the collocated grid used in OpenFOAM. p denotes pressure and ρ denotes density.

$$\frac{\rho^{n+1}U^{n+1} - \rho^n U^n}{\Delta t} + \frac{1}{V_{cell}} \sum_f S_f(\rho_f^{n+1} U_f^{n+1} U_f^{n+1}) =$$

$$- \frac{1}{V_{cell}} \int_{V_{cell}} \frac{dp^{n+1}}{dx} dV + \frac{1}{V_{cell}} \sum_f S_f \mu_f \frac{dU}{dx}\bigg|_f, \quad (4.2)$$

$$\frac{\rho^{n+1} - \rho^n}{\Delta t} + \frac{1}{V_{cell}} \sum_f (\rho_f^{n+1} U_f^{n+1}) = 0, \quad (4.3)$$

where $\rho(\mathbf{x}, t)$ is the gas phase density and $\mathbf{u}(\mathbf{x}, t)$ is the velocity vector. where p is the pressure, μ is the viscosity, and I is the Kronecker delta function expressed as a vector. In addition, transport equations for a set of species that describe the thermochemical composition vector need to be solved. Note that the pressure term of the momentum equation is kept in the integral form since the formulation of the pressure equation will not involve the pressure itself, but only the pressure gradient.

In the low-Mach number solver, density is obtained form the species equations. This is particularly useful with flamelet-based models, where the progress variable is used to look-up density from the table. Consequently, the continuity equation is solved only indirectly to enforce mass balance. Hence, the main issue in low-Mach number solvers is the consistent implementation of this external density input from a table. Here, we will start from the semi-implicit fractional time-step method described in [40] and [28].

The algorithm is based on an uncoupled approach, where the transport equations are solved sequentially and not simultaneously. To enforce consistency at the next time-step, an inner iterative loop is executed. For reference, superscript n refers to time-step and subscript m refers to solution at some inner-iteration level. Note that in a collocated mesh, the values of the variables are stored at cell center. OpenFOAM computes the face values only for

temporary use. The subscript f refers to face values, which are computed using linear interpolation. Any interpolated variable is also denote by by $\bar{\cdot}$. For velocity, an intermediate time is also needed (in-between iterations), which is denoted by $\cdot^{*}$.

The time-stepping algorithm based on [40] and [28] is as follows:

1) Obtain ϕ_m^{n+1} from the scalar transport equation

For the scalar equation the inlet boundary condition can usually be fixed to a certain value and if the outlet is far enough from from any flow variations, it can be assumed that the last cell center value for the scalar is the same as the last face value (zero-gradient assumption).

$$\frac{1}{V_{cell}} \frac{\rho_{m-1}^{n+1} \phi_m^{n+1} - \rho^n \phi^n}{\Delta t} + \sum S_f \Phi_{f,m-1}^{n+1} \overline{\phi_{f,m}^{n+1}} =$$
$$\sum S_f \overline{(\rho D)_{f,m-1}^{n+1}} (\nabla \phi_m^{n+1})_f + \dot{\omega}, \quad (4.4)$$

where V_{cell} denotes the volume of the finite-volume cell, S_f is the surface area of the face and Φ is the mass flux based on an interpolation of ρU at the cell faces. Note that the equation solved for ϕ and not $\rho\phi$, since this allows the diffusion term to be treated implicitly.

2) Update density and thermophysical properties based on the updated scalar field ϕ_m^{n+1}

$$D_m^{n+1} = f(\phi_m^{n+1}), \quad \rho_m^{n+1} = f(\phi_m^{n+1}) \quad \mu_m^{n+1} = f(\phi_m^{n+1}) \tag{4.5}$$

3) Update momentum equation and enforce continuity

The boundary conditions for velocity can be the same as the scalar equation. At the outflow, it is also common to use the convective boundary condition that is useful in removing vortical elements [12].

$$\frac{\partial \psi}{\partial t} + u_c \frac{\partial \psi}{\partial n} = 0, \tag{4.6}$$

where ψ denotes the quantity which follows the transport equation solved for. ψ can denote a transported scalar or different components of the transported vector.

With the fractional timestep method, the velocity is first advanced from the previous timestep to a fractional timestep writing the so-called fractional momentum equation.

$$\frac{\rho_{m-1}^{n+1} U_m^* - \rho^n U^*}{\Delta t} V_{cell} + \sum S_f \Phi_{f,m-1}^{n+1} \overline{U_{f,m}^*} = \sum S_f \overline{D_{f,m-1}^{n+1}} (\nabla U_m^*)_f \tag{4.7}$$

Note here that instead, boundary conditions for the fractional velocity should be provided, based on the previous description of the boundaries for the non-fractional velocity. This approximation has been shown to be first order accurate in time [28].

The fractional velocity U^* will have been computed at the cell center such that the fractional momentum conservation equation is enforced. The momentum transport equation is then completed by taking int account a fluctuating pressure gradient. Because mass conservation also need to be enforced, the pressure fluctuation is computed such that mass conservation equation is enforced in each cell.

For the fluctuating pressure p, the boundary conditions are not straightforward, mainly because the pressure that is computed is a fluctuating pressure

43

which has no physical meaning. Even though different equations can be specified for pressure, as we will see below, they are all elliptic equations. A fixed gradient for pressure is specified at all boundaries that will bridge the gap between the non-mass-conservative field U^* and the mass conservative field U. Therefore, a null gradient is imposed where velocity does not need to be corrected. Since the inlet velocity is usually known, an average outlet velocity can also be obtained based on a global mass conservation analysis. The boundary conditions for U^* can then be specified such that its last face has the mass conservative flux. Then fluctuating pressure field can be solved with a null gradient at the inlet and outlet faces. This approach also allows to get a prediction of the velocity at the last face which is useful for convective velocity boundary conditions.

This pressure correction approach could be obtained in different ways within OpenFOAM, which are discussed below. To simplify the notations, we will denote the convection term as $\mathcal{C}$ and the diffusion term as $\mathcal{D}$. The superscript and subscript associated with each of this term determines which updated value of velocity is used in each of these terms.

3)a) Explicit Momentum method

Here the convection and diffusion part of the momentum equation are treated explicitly using the most recent update of the solver. More precisely, the fractional momentum equation is written as

$$\frac{(\rho U)^* - \rho^n U^n}{\Delta t} + \mathcal{C}_{m-1}^{n+1} = \mathcal{D}_{m-1}^{n+1} \tag{4.8}$$

Note that here there is no need to separate ρ^* and U^*. The pressure component is added as follows.

$$\frac{(\rho U)^{n+1} - (\rho U)^*}{\Delta t} = -\nabla p, \tag{4.9}$$

where p is the fluctuating pressure. Taking the divergence of the above equation along with the following discrete version of the continuity equation

$$\frac{\partial \rho^{n+1}}{\partial t} + \nabla \cdot ((\rho U)^{n+1}) = 0, \tag{4.10}$$

leads to the elliptic equation for pressure:

$$\nabla^2 p = \frac{1}{\Delta t}\left(\frac{\partial \rho_m^{n+1}}{\partial t} + \nabla \cdot ((\rho U)^*)\right). \tag{4.11}$$

3)b) Implicit method with pressure accumulation

In the previous method, the pressure is updated each step and there is no time-dependency to this quantity. In the second approach that follows, pressure is accumulated over time iterations and outer iterations. Since pressure is being accumulated, the correction between the non-mass-conservative mass flux given by the interpolation of $\rho_m^{n+1} U^*$ at the faces and the mass conservative mass flux Φ_m^{n+1} tends to zero. The convection and diffusion part of the fractional momentum equation which use the non-mass-conservative flux $\rho_m^{n+1} U^*$ can be then be considered to be treated implicitly after enough outer iterations. This leads to the following pressure-included version

$$\frac{(\rho U)^* - \rho^n U^n}{\Delta t} + \mathcal{C}^* = -\nabla p_{m-1}^{n+1} + \mathcal{D}^*. \tag{4.12}$$

The iterative scheme then proceeds as follows:

$$\frac{(\rho U)^{n+1} - \rho^n U^n}{\Delta t} + \mathcal{C}^* = \mathcal{D}^*, \tag{4.13}$$

$$\frac{(\rho U)^{n+1} - \rho^n U^n}{\Delta t} + \mathcal{C}^* = \mathcal{D}^* - \nabla \delta p, \tag{4.14}$$

and

$$\nabla^2 \delta p = \frac{1}{\Delta t}\left(\frac{\partial \rho_m^{n+1}}{\partial t} + \nabla \cdot ((\rho U)^*)\right) \tag{4.15}$$

45

The fluctuating pressure p is corrected as

$$p_m^{n+1} = p_{m-1}^{n+1} + \delta p \qquad (4.16)$$

3)c) OpenFOAM's Implicit method

In OpenFOAM two operators $\mathcal{A}$ and $\mathcal{H}$ have been implemented to treat this problem (section 3.8.1 in [25]). The complete momentum equation is written as follows:

$$\mathcal{A}U - \mathcal{H} = -\nabla p, \qquad (4.17)$$

where U now refers to the vector of velocity values. $\mathcal{A}$ is the diagonal part of the discretization operator, and $\mathcal{H}$ is the off-diagonal part of the same operator. Based on this discrete version, the ractional time step method momentum equation can be written as:

$$\mathcal{A}^*.U^* = \mathcal{H}. \qquad (4.18)$$

A non-mass-conservative mass flux can be defined as $\Phi^* = \overline{\rho_m^{n+1} U^*}$. The complete momentum equation is then written as:

$$\mathcal{A}^{n+1}.U_m^{n+1} = \mathcal{H} - \nabla p_m^{n+1} \qquad (4.19)$$

The most updated density is used for both equations, and since the spatial schemes are kept identical

$$\mathcal{A}^{n+1} = \mathcal{A}^* = \mathcal{A}. \qquad (4.20)$$

This results in the following Poisson equation for the fluctuating pressure p

$$\nabla \cdot (\rho_m^{n+1} \mathcal{A}^{-1} \nabla p_m^{n+1}) = \frac{\partial \rho^{n+1}}{\partial t} + \nabla \cdot (\Phi^*) \qquad (4.21)$$

This method is the one selected for the current solver because it recognizes that the fluctuating pressure has to correct not only Φ^*, but also $\mathcal{C}^*$ and $\mathcal{D}^*$.

Using the operator $\mathcal{A}$ also allows more flexibility in the choice of time-stepping scheme.

4) Update the velocity field

Based on the solution of the Poisson equation, the velocity is updated as follows:

$$U_m^{n+1} = U^* - \mathcal{A}^{-1}.\nabla p_m^{n+1} \tag{4.22}$$

The pressure p obtained is such that mass conservation is enforced on each cell. More precisely, the gradient of pressure at the cell faces has been calculated to bridge the gap between cell faces values of $\rho_m^{n+1} U^*$ and the mass conserving cell faces values of Φ_m^{n+1}.

4.3 Impact of staggering for the correction of mass fluxes

It is important to discuss the difference between staggered and collocated meshes when applying the pressure correction to the fractional time velocity field. When the gradients in velocity are small, it is expected that the corrections will also be small and close to zero. For instance, if the outflow is associated with very small gradients,.

$$\nabla^2 p_{LastCell} = 0 \tag{4.23}$$

In a staggered code like NGA, the pressure is only specified at the cell centers. As seen in Fig. 4.3, the Poisson equation solved imposes a local gradient of pressure at the cell face $i - \frac{1}{2}$, which is the correction necessary to ensure mass conservation in the domain. Since the outflow velocity at the boundary has already been corrected to ensure global mass conservation, no more correction is required closer to the boundary.
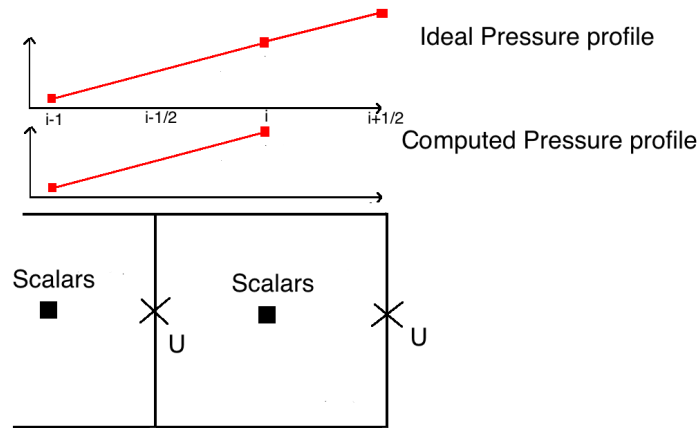
Figure 4.3: Illustration of the pressure correction process at the outflow boundary for a staggered discretization scheme.

In a collocated code such as OpenFOAM, the pressure is specified at the cell centers but also at the last face to express the boundary conditions. As seen in Fig. 4.4, like in the previous case, the Poisson equation solved imposes a local gradient of pressure at the cell face $i-\frac{1}{2}$, which is the necessary correction to ensure mass conservation in the domain. The velocity at the last face is also kept identical for the same reason as the staggered case. However, since the velocity is stored at the cell centers and not at the cell faces, an interpolation of the pressure gradient to the cell centers has to be made. Inside the domain, because the pressure gradients should be nearly continuous and smooth, the interpolation error is small. At the outlet however, the interpolated pressure gradient at the last cell center will always be averaged with the zero pressure gradient prescribed at the boundary. It implies that the correction applied for the velocity at the last cell center is underestimated compared to the neighbors
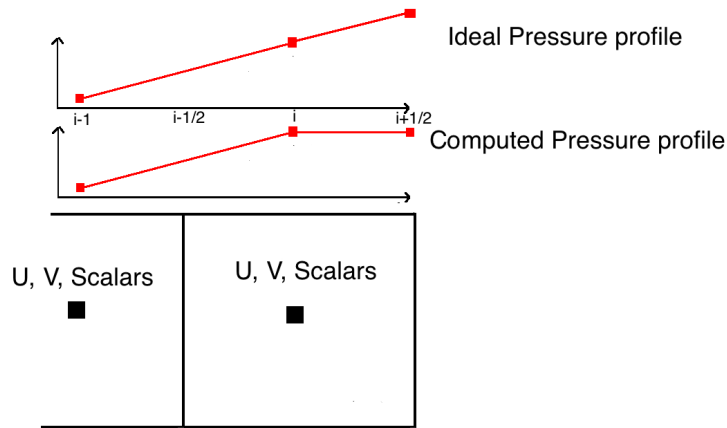
Figure 4.4: Illustration of the pressure correction process at the outflow boundary for a collocated discretization scheme.

which can create oscillations for the flow field. This will be illustrated with the verification case in the Section 4.5.

4.4 Verification using a method of manufactured solutions (MMS)

The code is tested using the 1-D MMS problem of [46]. The objective is to verify the solver implementation and to understand the convergence properties of the algorithm described in the previous section. In the MMS approach, source terms are added to the 1D equations such that an analytic representation of the solutions is made possible. The analytic solutions for the 1D case used here can be found in [46]. For the variable density case, a density ratio of 10 is used as it is typical of combustion applications. The

corresponding analytical solutions are shown as a function of time in Fig. 4.5.
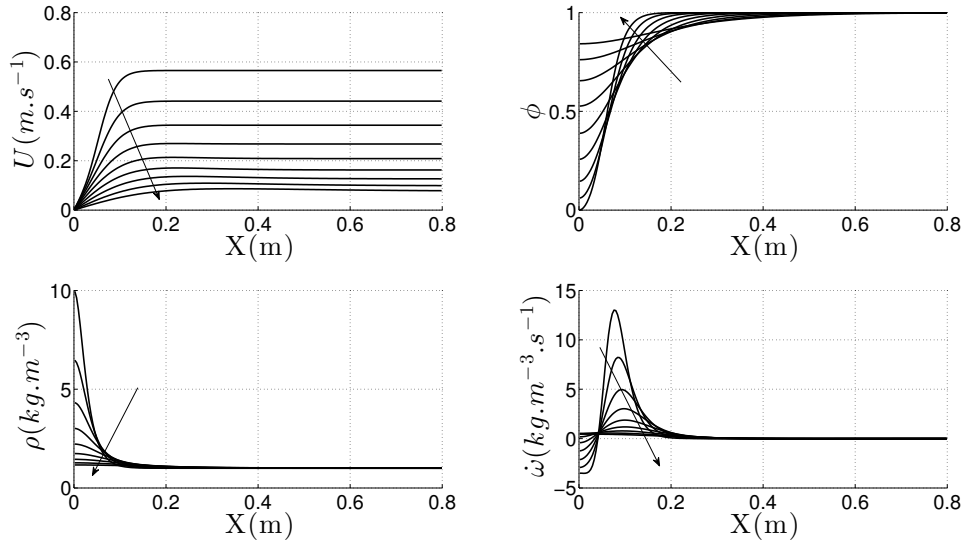

Figure 4.5: Analytical solutions of the 1D MMS problem. The arrows point in the direction of increasing time from 0 to 1s.

A suite of simulations were run with different grid resolutions to test convergence properties (Fig. 4.9 and Fig. 4.8) The grid sizes ranged from 64 to 2048 cells for a 2m domain. For the lowest resolution case (64 cells), significant pressure oscillations were found inside the domain. This is related to the pressure extrapolation problem discussed in Section 4.3. Due to the low resolution, the oscillations are present far inside the domain, away from the boundaries. This is essentially due to a large change in pressure gradients across two neighboring cell faces. More precisely, when applying a pressure correction for the conservation of mass, the gradient of pressure modifies the velocity at the cell faces. For consistency between the cell face velocities and the cell center velocities, this correction is also applied at the cell centers. However, nothing guarantees that this operation will enforce the velocity at
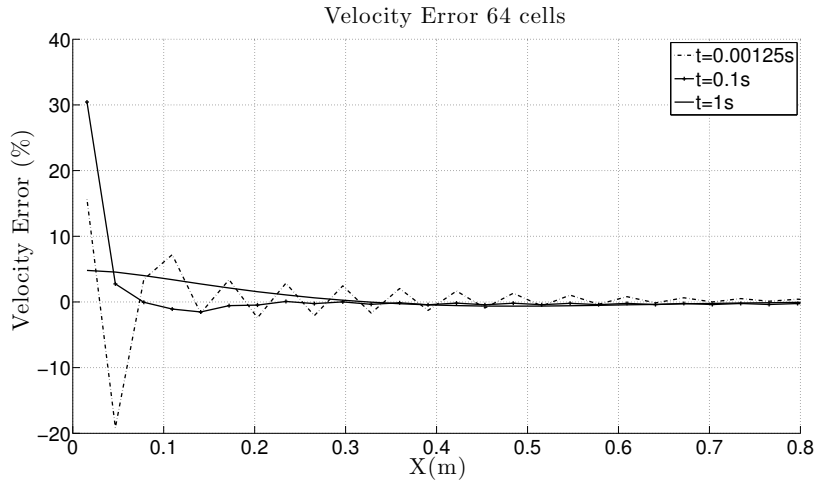
Figure 4.6: Error between the computed and the analytic velocity profiles at different timesteps.

the cell centers to be the velocity interpolated from the cell faces. Fortunately, this problem diminishes as the grid is refined.

There is also an interesting aspect of the transient evolution. It was found that even if the computed solution exhibits significant errors after the first few steps, this error was found to decrease with time. This may be due to the fact that the analytical solution contains a diffusive component that decreases the gradients with time (Fig. 4.5. However, this does not imply that accumulation of errors is not important in general.

In the scalar error profiles (Fig. 4.7, it can be noticed that the coarser simulations exhibit a large error very close to the location where the scalar source term is applied. This is mainly due to the discretization of the analytic source term function, and problem becomes less important for more refined meshes. Overall, the solver is reasonably accurate in capturing the analytic solution, with peak errors less than 10% at all times and at all spatial locations
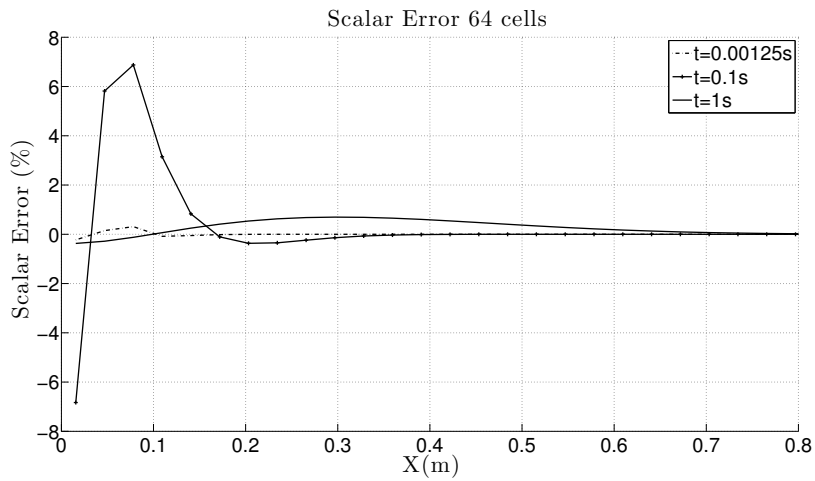
Figure 4.7: Error between the computed and the analytic scalar profile at different timesteps.

for adequately resolved meshes.

To further understand convergence, the $L2$ norm and $L - \infty$ norm of the solution is plotted as a function of grid spacing in Fig. 4.8. For these cases, the time-step is held very small in order to remove inaccuracies due to the temporal scheme. The scalar field shows a second-order convergence while the velocity field Fig. 4.9 shows a slightly lower order of convergence, probably due to the projection algorithm being sensitive to the density gradients in the flow.

Figure 4.10 shows the change in the order of convergence as a function of time. It is seen that the accumulation of error affects the velocity field more than the scalar field, with a steeper drop in convergence order.
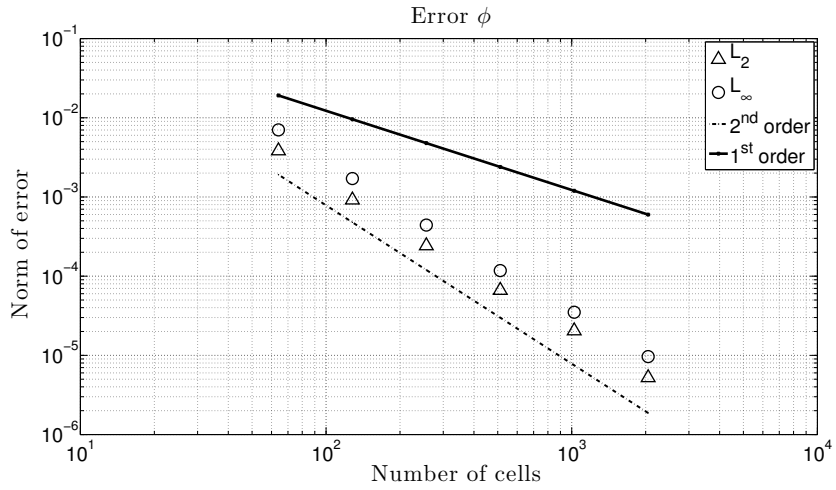
52

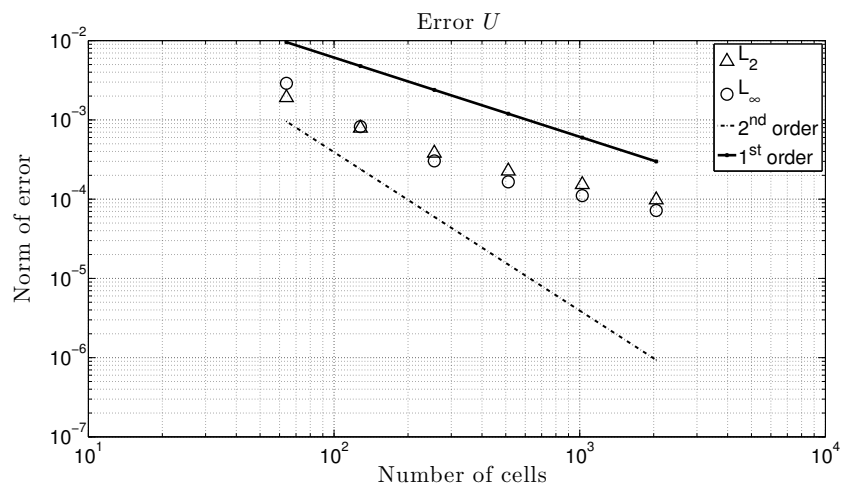Figure 4.8: Computed order of convergence for the scalar ϕ field.

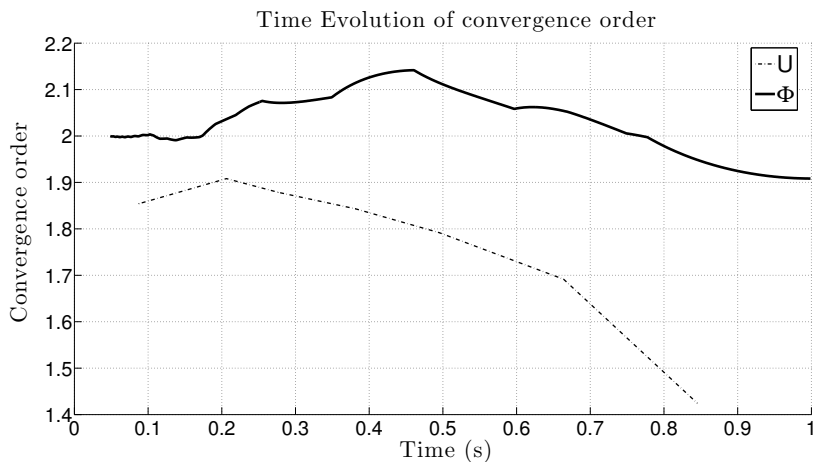Figure 4.9: Computed order of convergence for the velocity U field.

Figure 4.10: Evolution as a function of time of the convergence order for U field with 64 cells.

4.5 Illustration of the outflow problem

As mentioned before, with a collocated solver, the correction applied at the outlet boundary is always underestimated. An inconsistency between neighbors corrections then appears and can result in spurious oscillations in the velocity field. This problem is illustrated with the 1D case studied for the code verification. Figure 4.11 shows the error in the velocity field at the outlet of the domain at the end of the first timestep. As expected, oscillations due to the non-uniform pressure correction applied can be observed. Note that the oscillations penetrate far into the domain due to the inner iterations. With each inner iteration, the fluctuation at the boundary is carried further into the domain. However, the amplitude of the oscillations are small compared to the average error found near the outlet (roughly 1.3%).

Figure 4.12 shows the same phenomenon at time $t = 1s$. It is seen that the oscillations persist and grow in magnitude relative to the average error.
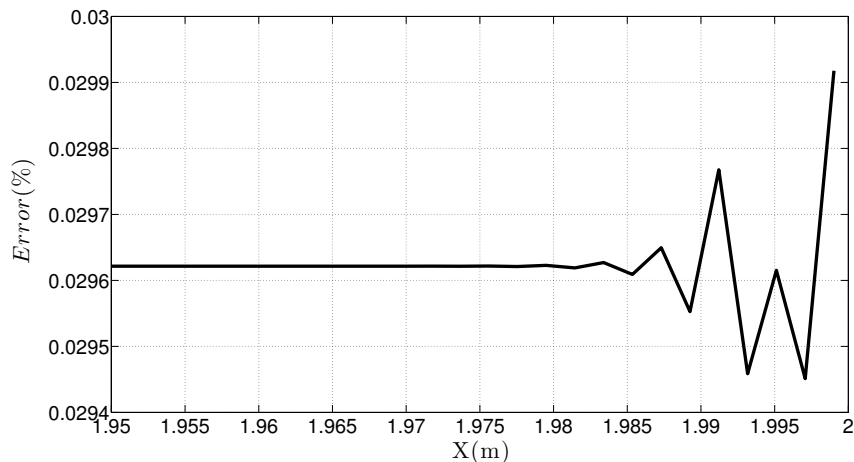
Figure 4.11: Error in the computed velocity field relative to the analytic solution at t=0.00125s plotted at the outflow boundary for the computation with 1024 cells.

While this might seem like a destabilizing component of the algorithm, it was found that in complex geometries the outflow problem could be minimized by using the convective boundary condition (Eq. 4.6). Hence, the current algorithm, in spite of these issues, was found to be robust for practical applications.

4.6 Application to complex geometries

The solver described in this chapter has been successfully implemented in the OpenFOAM package and used to simulate a number of complex flow configurations. Here, two examples from related projects are shown to demonstrate the applicability of this method. Figure 4.13 shows an LES computation of a model gas turbine combustor with secondary oxidizing air being injected downstream of the main reaction zone. This flow configuration consists of swirling flow with density change, low aspect-ratio regions of computational
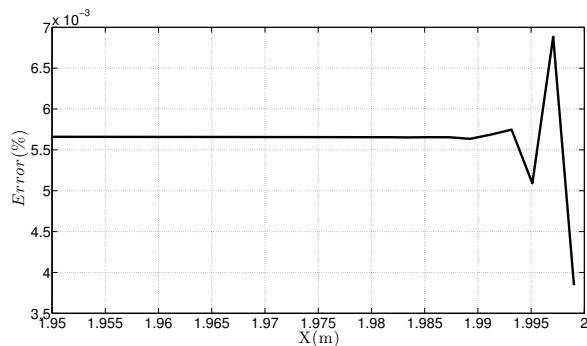
Figure 4.12: Error in the computed velocity field relative to the analytic solution at t=1s plotted at the outflow boundary for the computation with 1024 cells.

mesh, multiple inlets and strong velocity changes close to the outflow. In spite of these challenges, the algorithm is stable and converges within a few inner iterations.

The second application is directly related to flashback application (Fig. 4.14. Here, a model swirl flow flashback studied at UT Austin is reproduced using the OpenFOAM solver. Similar to the gas turbine combustor application, this geometry involves complex features and strong variations in the density and velocity across different regions of the mesh. Similar to the previous case, the low-Mach number algorithm was found to be stable.

Figure 4.13: Isocontour of progress variable based on species mass fraction in a multiple injection combustor, colored by axial velocity. Courtesy of Dr. Heeseok Koo [30].
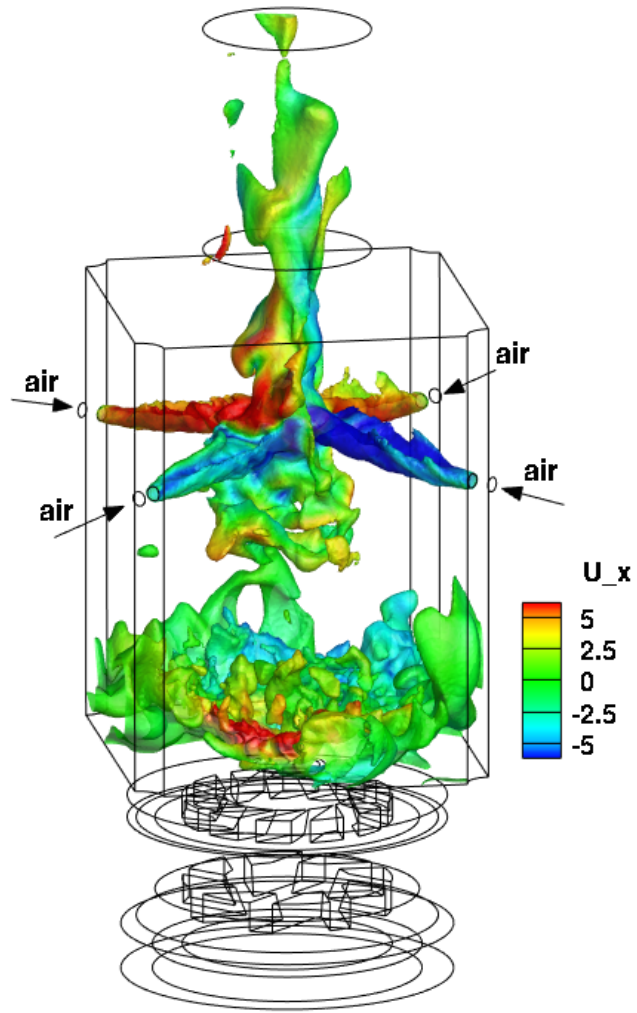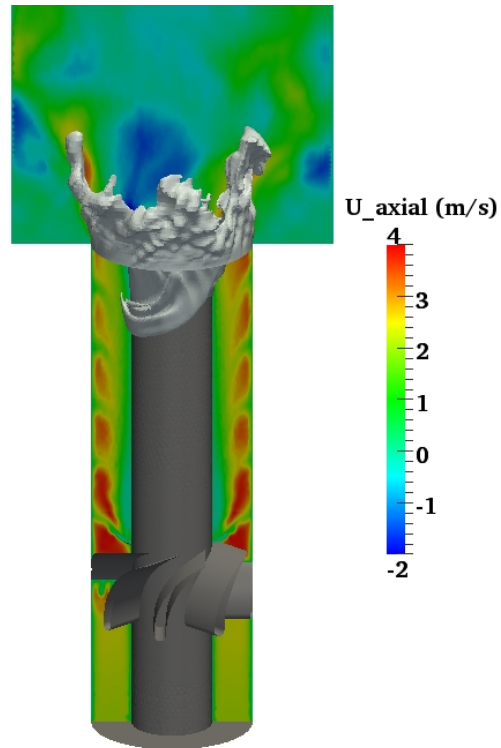
Figure 4.14: Isocontour of progress variable based on species mass fraction, with a colored field of axial velocity obtained during flashback of a premixed swirling flame in a model combustor. Courtesy of Mr. Christopher Lietz [35].

Bibliography

[1] K. Akselvoll and P. Moin. Large eddy simulation of turbulent confined coannular jets. *Journal of Fluid Mechanics*, 315:387–411, 1996.

[2] P. Auzillon, B. Fiorina, R. Vicquelin, N. Darabiha, O. Gicquel, and D. Veynante. Modeling chemical flame structure and combustion dynamics in les. In *Proceedings of the Combustion Institute*, volume 33, pages 1331–1338, 2011.

[3] R. W. Bilger. Conditional moment closure for turbulent reacting flow. *Physics of Fluids*, 5(2):436–444, February 1993.

[4] F. Bisetti, G. Blanquart, M. E. Mueller, and H. Pitsch. On the formation and early evolution of soot in turbulent nonpremixed flames. *Combustion and Flame*, 159:317–335, 2012.

[5] M. Boger, D. Veynante, H. Boughanem, and A. Trouve. Direct numerical simulation analysis of flame surface density concept for large eddy simulation of turbulent premixed combustion. *Twenty-Seventh Symposium (International) on Combustion*, 27:917–925, 1998.

[6] R. Borghi and M. Destriau. *Combustion and Flames*. Editions Technip, 1998.

[7] F. Colin, F. Ducros, D. Veynante, and T. Poinsot. A thickened flame model for large-eddy simulation of premixed turbulent combustion. *Physics of Fluids*, 12(7):1843–1863, 2000.

[8] P. E. Desjardin and S. H. Frankel. Large eddy simulation of a non-premixed reacting jet: Application and assessment of subgrid-scale combustion models. *Physics of Fluids*, 10:2298–2314, 1998.

[9] O. Desjardins, G. Blanquart, G. Balarac, and H. Pitsch. High order conservative finite difference scheme for variable density low Mach number turbulent flows. *Journal of Computational Physics*, 227(15):7125–7159, JUL 20 2008.

[10] C. Eichler and T. Sattelmayer. Experiments on flame flashback in a quasi-2d turbulent wall boundary layer for premixed methane-hydrogen-air mixtures. *Journal of Engineering for Gas Turbines and Power*, 133, 2011.

[11] Christian T. Eichler. *Flame Flashback in Wall Boundary Layers of Premixed Combustion Systems.* PhD thesis, Technische Universität München, 2011.

[12] J. H. Ferziger and M. Peric. *Computational Methods for Fluid Dynamics.* Springer, 3rd edition, 2002.

[13] B. Fiorina, O. Gicquel, L. Vervisch, S. Carpentier, and N. Darabiha. Approximating the chemical structure of partially premixed and diffusion counterflow flames using FPI flamelet tabulation. *Combustion and Flame*, 140:147–160, 2005.

[14] B. Fiorina, R. Vicquelin, P. Auzillon, N. Darabiha, O. Gicquel, and D. Veynante. A filtered tabulated chemistry model for les of premixed combustion. *Combustion and Flame*, 157:465–475, 2010.

[15] R. O. Fox. *Computational Models for Turbulent Reacting Flows.* Cambridge University Press, Cambridge, 2003.

[16] R. O. Fox and V. Raman. A multienvironment conditional probability density function model for turbulent reacting flows. *Physics of Fluids*, 16(12):4551–4565, 2004.

[17] M. Germano. Turbulence : The filtering approach. *Journal of Fluid Mechanics*, 286:229–255, 1991.

[18] A. Gruber, J. H. Chen, D. Valiev, and C. K. Law. Direct numerical simulation of premixed flame boundary layer flashback in turbulent channel flow. *Journal of Fluid Mechanics*, 709:516–542, 2012.

[19] F. Hernandez-Perez, F. Yuen, C. Groth, and O.L. Gulder. Les of a laboratory-scale turbulent premixed bunsen flame using fsd, pcm-fpi, and thickened flame models. In *Proceedings of the Combustion Institute*, volume 33, pages 1365–1371, 2011.

[20] M. Herrmann, G. Blanquart, and V. Raman. A bounded quick scheme for preserving scalar bounds in large-eddy simulations. *AIAA Journal*, 44(12):2879–2880, 2006.

[21] C. Heye, V. Raman, and A. R. Masri. LES/PDF approach for the simulation of an ethanol spray flame. *Proceedings of the Combustion Institute*, 34.

[22] C. Heye, V. Raman, and Masri A. R. Influence of spray/combustion interactions on auto-ignition of methanol spray flames. *Proceedings of the Combustion Institute*, 2015.

[23] M. Ihme, L.Shunn, and J. Zhang. Regularization of reaction progress variable for application to flamelet-based combustion models. *Journal of Computational Physics*, 231:7715–7721, 2012.

[24] J. Janicka, W. Kolbe, and W. Kollmann. Closure of the transport equation for the PDF of turbulent scalar fields. *Journal of Non-Equilibrium Thermodynamics*, 4:47–66, 1970.

[25] Hrvoje Jasak. *Error Analysis and Estimation for the Finite Volume Method with Applications to Fluid Flows*. PhD thesis, Imperial College of London, 1996.

[26] C. M. Kaul and V. Raman. A posteriori analysis of numerical errors in subfilter scalar variance modeling for large eddy simulation. *Physics of Fluids*, 23(3), MAR 2011.

[27] A. Kempf, R. P. Lindstedt, and J. Janicka. Large-eddy simulation of bluff-body stabilized nonpremixed flame. *Combustion and Flame*, 144(1-2):170–189, 2006.

[28] J. Kim and P. Moin. Application of a fractional-step method to incompressible Navier-Stokes equations. *Journal of Computational Physics*, 59(2):308–323, 1985.

[29] A. Yu. Klimenko. Note on the conditional moment closure in turbulent shear flows. *Physics of Fluids*, 7(2):446–448, February 1995.

[30] H. Koo, V. Raman, M. Mueller, and Geigle K. P. Large-eddy simulation of a turbulent sooting flame in a swirling combustor. In *53rd AIAA Aerospace Science Meeting*, 2015.

[31] V. Kurdyumov, E. Fernandez-Tarrazo, and A. Linan. Flame flashback and propagation of premixed flames near a wall. In *Proceedings of the Combustion Institute*, volume 28, pages 1883–1889, 2000.

[32] V. Kurdyumov, E. Fernandez-Tarrazo, J. M. Truffaut, J. Quinard, A. Wangher, and G. Searby. Experimental and numerical study of premixed flame flashback. In *Proceedings of the Combustion Institute*, volume 31, pages 1275–1282, 2007.

[33] G. Lewis. Centrifugal-force effects on combustion. *Proceedings of the Combustion Institute*, 14, 1973.

[34] J. Li, Z. Zhao, A. Kazakov, and F. Dryer. An updated comprehensive kinetic model of hydrogen combustion. *International Journal of Chemical Kinetics*, 36:566–575, 2004.

[35] C. Lietz and V. Raman. Large-eddy simulation of flashback in a swirling premixed flame. In *53rd AIAA Aerospace Science Meeting*, 2015.

[36] P. Moin, K. Squires, W. Cabot, and S. Lee. A dynamic subgrid-scale model for compressible turbulence and scalar transport. *Physics of Fluids A*, 3:2746–2757, 1991.

[37] M. E. Mueller and H. Pitsch. Large eddy simulation of soot evolution in an aircraft combustor. *Physics of Fluids*, 25, 2013.

[38] Norbert Peters. *Turbulent Combustion*. Cambridge University Press, 2000.

[39] C. D. Pierce and P. Moin. Progress-variable approach for large-eddy simulation of non-premixed turbulent combustion. *Journal of Fluid Mechanics*, 504:73–97, 2004.

[40] Charles D. Pierce. *Progress-variable approach for large-eddy simulation of turbulence combustion*. PhD thesis, Stanford University, 2001.

[41] H. Pitsch. A C++ computer program for 0-d and 1-d laminar flame calculations. RWTH Aachen, 1998.

[42] H. Pitsch. Large-eddy simulation of turbulent combustion. *Annual Review of Fluid Mechanics*, 38:453–482, 2006.

[43] S. B. Pope. Computations of turbulent combustion: Progress and challenges. In *Proceedings of the 23rd Symposium (International) on Combustion*, pages 591–612. The Combustion Institute, Pittsburgh, 1990.

[44] S. B. Pope. *Turbulent Flows*. Cambridge University Press, 2000.

[45] V. Raman, H. Pitsch, and R. O. Fox. A consistent hybrid LES-FDF scheme for the simulation of turbulent reactive flows. *Combustion and Flame*, 143(1-2):56–78, 2005.

[46] L. Shunn, F. Ham, and P. Moin. Verification of variable-density flow solvers using manufactured solutions. *Journal of Computational Physics*, 231:3801–3827, 2012.

[47] J. Smagorinsky. General circulation experiments with the primitive equations: I. the basic equations. *Monthly Weather Review*, 91:99–164, 1963.

[48] Y. Sommerer, D. Galley, T. Poinsot, S. Ducruix, F. Lacas, and D. Veynante. Large eddy simulation and experimental study of flashback and blow-off in a lean partially premixed swirled burner. *Journal of Turbulence*, 5(37), 2004.

[49] G. Tabor and H.G. Weller. Large eddy simulation of premixed turbulent combustion using xi-flame surface wrinkling model. *Flow, Turbulence and Combustion*, 72:1–28, 2004.

[50] E. Tangermann and M. Pfitzner. Evaluation of combustion models for combustion-induced vortex breakdown. *Journal of Turbulence*, 10(7):1–21, 2009.

[51] D. Thibaut and S. Candel. Numerical study of unsteady turbulent premixed combustion: application to flashback simulation. *Combustion and Flame*, 113:53–65, 1998.

Vita

Malik Hassanaly was born in Epinay-sur-Seine, a suburb of Paris in France on March 24th of 1992. He obtained his high-school diploma with High Honor and spent his freshman and sophomore years at the *Lycée Janson de Sailly* (Paris, France) in *Classes Préparatoires aux Grandes Ecoles*, a two-years program preparing for the national engineering graduate school entrance examination. He was then accepted at the *Ecole Centrale de Lille* (Villeneuve d'Ascq, France), where he was selected for the dual-degree program in collaboration with The University of Texas at Austin, and admitted to the Aerospace graduate program at UT. He is currently pursuing a PhD degree at the University of Michigan in Ann Arbor.

Permanent address: FXB Building 1320 Beal Ave
                                Ann Arbor, Michigan 48109

This thesis was typeset with LaTeX[†] by the author.

[†]LaTeX is a document preparation system developed by Leslie Lamport as a special version of Donald Knuth's TeX Program.